
Photo-Induced Phase Transition in RbMnFe Prussian Blue Analog-Based Magnet

H. Tokoro and S. Ohkoshi

1.1 Introduction

Studies that are related to temperature-induced phase transitions and photo-induced phase transitions are extensively investigated in solid-state chemistry [1–4]. Temperature-induced phase transition phenomena are observed in spin crossover or intramolecular electron transfer. In a spin crossover complex, a transition metal ion can be in either the low-spin or the high-spin state depending on the strength of the ligand field. When the thermal energy is close to the exchange energy that corresponds to the crossover, a spin transition occurs between the two spin states. This phenomenon is observed in octahedral coordinate iron transition metal complexes [5–7]. Charge-transfer phase transitions have been observed in mixed-valence complexes [7–13], e.g., $[M^{III}_2M^{II}O(O_2C_2H_3)_6L_3]$ ($M = Fe, Mn$; $L = H_2O, pyridine$) [12] and $M(dta)_4I$ ($M = Ni, Pt$; $dta = dithioacetato$) [13]. Charge-transfer phase transitions that accompany spin crossovers have also been reported, e.g., $Co(py_2X)(3,6-DBQ)_2$ ($X = O, S, Se$) [14] and $Na_{0.4}Co_{1.3}[Fe(CN)_6] \cdot 4.9H_2O$ [15]. A temperature-induced phase transition often accompanies a thermal hysteresis loop, which is related to the cooperativity of the corresponding system. The cooperativity in a metal complex assembly is due to the interaction between a metal ion and lattice strain, e.g., an electron-phonon coupling [16], a Jahn–Teller distortion [17], and an elastic interaction [18]. Cyano-bridged metal assemblies such as hexacyanometalate- [4, 19–38] and octacyanometalate-based magnets [39–44] are suitable for observing a thermal phase transition since they are mixed-valence compounds that have a strong cooperativity due to the CN ligand bridges.

To date, several types of photo-induced phase-transition phenomena have been reported, for example, a light-induced crystalline-amorphous transformation in chalcogenide material [45–47], a light-induced spin-state change on the transition metal ion of a metal complex [3, 48, 49], a light-induced charge transfer in donor-accepter stacked molecules [2, 50, 51], ferromagnetic bimetallic assemblies [35–44], or perovskite manganite [52, 53]. Until now,

we have demonstrated photomagnetic effects such as photo-induced magnetization and the photo-induced magnetic pole inversion with cyano-bridged bimetallic assemblies [4, 35, 38–44]. One possible method for achieving optical control of magnetization is to change the electron spin state of a magnetic material. For example, if photo-irradiation varies the oxidation numbers of transition metal ions within a magnetic material, its magnetization will be controlled. The bistability of the electronic states is also indispensable for observing photo-induced persistent magnetization since the energy barrier between these bistable states can maintain the photo-produced state even after photo-irradiation is ceased.

From this viewpoint, Prussian blue analogs are an attractive system due to their high T_c values [22]. In particular, Verdaguer et al. reported that $V^{II}[Cr^{III}(CN)_6]_{0.86} \cdot 2.8H_2O$ exhibits a T_c value of 315 K [24]. Successively, Girolami et al. and Miller et al. reported crystalline $K^IV[Cr^{III}(CN)_6]$ with $T_c = 103^\circ C$ and amorphous $K^I_{0.058}V^{II/III}[Cr^{III}(CN)_6]_{0.79}(SO_4)_{0.058} \cdot 0.93H_2O$ with $T_c = 99^\circ C$ powder, respectively [27, 28]. In multi-metal Prussian blue analogs, the rational design of magnets based on the molecular field theory is possible for the following reasons: (1) metal substitutions induce only small changes in the lattice constant and (2) superexchange interactions are only essentially effective between the nearest neighbor metal ions [25]. For example, we have designed a novel type of magnet that exhibits two compensation temperatures with the system of $(Ni^{II}_{0.22}Mn^{II}_{0.60}Fe^{II}_{0.18})_{1.5}[Cr^{III}(CN)_6] \cdot 7.5H_2O$ i.e., the spontaneous magnetization changes sign twice as the temperature is varied [29]. In this study, we show the temperature-induced phase transition and photo-induced phase transition of ferromagnetic $Rb_xMn[Fe(CN)_6]_{(x+2)/3} \cdot zH_2O$ complex.

1.2 Synthesis of Rubidium Manganese Hexacyanoferrate

Preparing method of rubidium manganese hexacyanoferrate, $Rb_xMn[Fe(CN)_6]_{(x+2)/3} \cdot zH_2O$, is as follows: an aqueous solution (0.1 mol dm^{-3}) of $Mn^{II}Cl_2$ with a mixed aqueous solution of Rb^ICl (1 mol dm^{-3}) and $K_3[Fe^{III}(CN)_6]$ (0.1 mol dm^{-3}) was reacted to yield a precipitate. The precipitate was filtered, dried, and yielded a powdered sample. The prepared compound was a light brown and elemental analyses for Rb, Mn, and Fe indicated that the obtained precipitate had a formula of $RbMn[Fe(CN)_6]$ ($x = 1, z = 0$). The 1: 1: 1 ratio of Rb: Mn: Fe allowed the Mn ions to coordinate six cyanonitrogens. Consequently, the network does not contain water molecules. Scanning electron microscope (SEM) images showed that the obtained powdered sample was composed of cubic microcrystals that were $2.1 \pm 1.1 \text{ }\mu\text{m}$. For the sample of different x , the sample was prepared by reacting an aqueous solution (0.1 mol dm^{-3}) of $Mn^{II}Cl_2$ with a mixed aqueous solution of Rb^ICl ($0.05\text{--}1 \text{ mol dm}^{-3}$) and $K_3[Fe^{III}(CN)_6]$ (0.1 mol dm^{-3}). The schematic structure of $Rb_xMn[Fe(CN)_6]_{(x+2)/3} \cdot zH_2O$ is shown in Fig. 1.1.

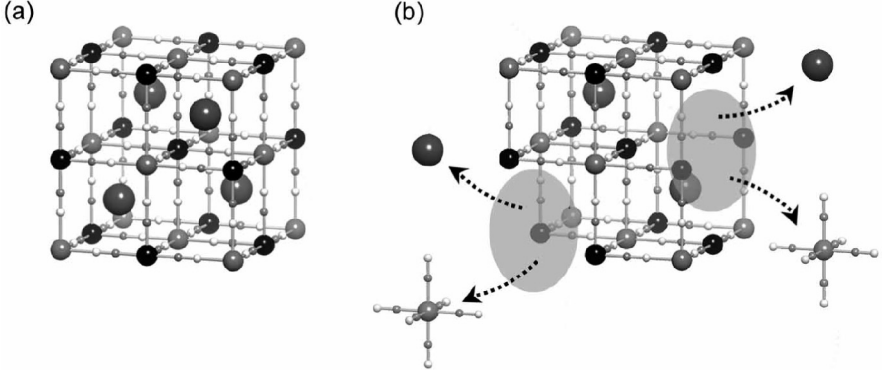


Fig. 1.1. Schematic structures of (a) $\text{Rb}^{\text{I}}\text{Mn}^{\text{II}}[\text{Fe}^{\text{III}}](\text{CN})_6$ and (b) $\text{Rb}_x^{\text{I}}\text{Mn}^{\text{II}}[\text{Fe}^{\text{III}}(\text{CN})_6]_{(x+2)/3} \cdot z\text{H}_2\text{O}$. Large gray circle is Rb^{I} ion, middle black circle is Mn^{II} ion, middle gray circle is Fe^{III} ion, small gray circle is C atom, and small white circle is N atom, respectively. Shadows indicate defects at the $\text{Fe}^{\text{III}}(\text{CN})_6$ sites. Water molecules are omitted for clarity

1.3 Crystal Structure of Rubidium Manganese Hexacyanoferrate

To study the crystal structure of rubidium manganese hexacyanoferrate, X-ray single crystal analysis was performed for $\text{Rb}_{0.61}\text{Mn}[\text{Fe}(\text{CN})_6]_{0.87} \cdot 1.7\text{H}_2\text{O}$ [54]. Crystal was obtained by the slow diffusion of MnCl_2 ($7 \times 10^{-3} \text{ mol dm}^{-3}$) dissolved in ethanol into $\text{K}_3[\text{Fe}(\text{CN})_6]$ ($3 \times 10^{-3} \text{ mol dm}^{-3}$) and RbCl ($1.4 \times 10^{-2} \text{ mol dm}^{-3}$) dissolved in water for three month. The obtained single crystals measured approximately $0.1 \times 0.1 \times 0.05 \text{ mm}^3$. Elemental analysis of Rb, Mn, and Fe of the single crystal was performed by microscopic fluorescent X-ray analysis (micro-FXA) with an X-ray spot size of $\varphi 10 \mu\text{m}$. The observed ratio of metal ions was $\text{Rb}:\text{Mn}:\text{Fe} = 0.58(\pm 0.04) : 1.00(\pm 0.03) : 0.86(\pm 0.03)$. The density (d) measured by the flotation method (tetrabromoethane and toluene) showed $d = 1.84(3) \text{ g cm}^3$. These results of micro-FXA and density measurements showed that the formula of the crystal was $\text{Rb}_{0.61}^{\text{I}}\text{Mn}^{\text{II}}[\text{Fe}^{\text{III}}(\text{CN})_6]_{0.87} \cdot 1.7\text{H}_2\text{O}$. Crystal data was collected on a Rigaku RAXIS RAPID imaging plate area detector with graphite monochromated Mo-K α radiation.

The present single crystal, $\text{Rb}_{0.61}\text{Mn}[\text{Fe}(\text{CN})_6]_{0.87} \cdot 1.7\text{H}_2\text{O}$, contains an intermediate composition value of 0.61 for Rb^+ . This compound has vacancies of $0.13 \times [\text{Fe}(\text{CN})_6]$ in the cubic lattice to maintain charge neutrality. It is expected that the Mn ion around the vacancy is coordinated to a water molecule (so-called ligand water) and the interstitial sites are occupied by Rb ions or non-coordinated waters (so-called zeolitic water molecules).

X-ray crystallography shows that $\text{Rb}_{0.61}^{\text{I}}\text{Mn}^{\text{II}}[\text{Fe}^{\text{III}}(\text{CN})_6]_{0.87} \cdot 1.7\text{H}_2\text{O}$ belongs to the face-centered cubic lattice $\text{Fm}\bar{3}\text{m}$ with lattice constants of

Table 1.1. Crystallographic and refinement data

Formula	Rb _{0.61} Mn[Fe(CN) ₆] _{0.87} ·1.7H ₂ O
Fw	322.1
Calculated density / g cm ⁻³	1.829
Temperature / K	93.1
Crystal system	Cubic
Space group	<i>Fm 3m</i>
Lattice constants / Å	10.5354(4)
Unit cell volume / Å ³	1169.37(8)
Number of formula units <i>Z</i>	4
Absorption coefficient μ / cm ⁻¹	46.66
Number of measured reflections	20363
Number of independent reflections	292
Number of refined parameters	15
GOF on $ F ^2$	1.270
<i>R</i> 1 [<i>I</i> > 2 σ (<i>I</i>)]	0.0449
w <i>R</i> 2	0.1081

$a = b = c = 10.5354(4)$ Å and $Z = 4$. The crystallographic agreement factors are $R1 = 0.0449$ [$I > 2\sigma(I)$] and $wR2 = 0.1081$ (Further details are available from the Fachinformationszentrum Karlsruhe, D-76344 Eggenstein-Leopoldshafen: crysdata@fiz-karlsruhe.de by quoting the depository number CSD 417499). Table 1.1 shows the crystal data and the refinement details. The asymmetric unit contained manganese atom [Mn(1)] at position 4a (0, 0, 0), iron atom [Fe(1)] at position 4b (1/2, 1/2, 1/2), rubidium atom [Rb(1)] at position 8c (1/4, 1/4, 1/4), cyanonitrogen [N(1)] and cyanocarbon [C(1)] at positions 24e (0.3174(4), 0, 0) and 24e (0.2068(4), 0, 0), respectively, oxygen atoms of the ligand water molecule [O(1)] at a vacancy, and oxygen atoms of zeolitic water molecule [O(2)] at position (0.369(4), 0.369(4), 0.369(4)) and [O(3)] at position (0.327(4), 0.327(4), 0.327(4)). Figure 1.2 shows the xy -plane of unit cell for the cubic network. All the cyanide groups exist as bridges between Mn(1) and Fe(1) in the three-dimensional framework. Mn(1) is connected to N(1) and O(1) for an average composition of MnN_{0.87}O_{0.13} due to the vacancy of [Fe(CN)₆]³⁻. The interatomic distances of Fe(1)–C(1), C(1)–N(1), and Mn(1)–N(1) [or Mn(1)–O(1)] are 1.9238(1), 1.1652(1), and 2.1786(1) Å, respectively. Rb(1) occupies the center of the interstitial sites, and O(2) and O(3) are distributed in a disordered fashion inside the Mn(1)–N(1) [or Mn(1)–O(1)] interstitial sites of the cubic network as zeolitic waters.

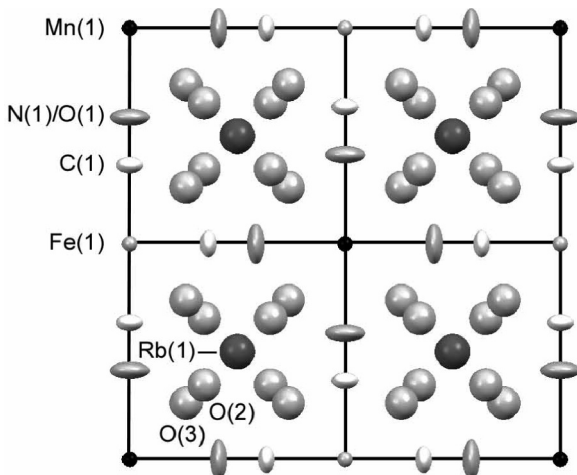


Fig. 1.2. Crystal structure for $\text{Rb}_{0.61}\text{Mn}[\text{Fe}(\text{CN})_6]_{0.87} \cdot 1.7\text{H}_2\text{O}$. The projection in the $-$ -plane (cubic, $\text{Fm}\bar{3}\text{m}$). Spheres and ellipsoids are drawn at a 50% probability level. All H atoms are omitted for clarify. Occupancies are 0.305 for Rb(1), 1.00 for Mn(1), 0.87 for Fe(1), 0.87 for C(1), 0.87 for N(1), 0.13 for O(1), 0.0528 for O(2), and 0.0624 for O(3), respectively

1.4 Temperature-Induced Phase Transition

1.4.1 Phase Transition Phenomenon in Magnetic Susceptibility

Figure 1.3 shows the product of the molar magnetic susceptibility (χ_M) and the temperature (T) vs. T plots of $\text{RbMn}[\text{Fe}(\text{CN})_6]$. The $\chi_M T$ value in the high-temperature (HT) phase is $4.67 \text{ cm}^3 \text{ K mol}^{-1}$ at 330 K, but cooling the sample at a cooling rate of 0.5 K min^{-1} decreases the $\chi_M T$ value around 235 K and at $T = 180 \text{ K}$ in the low-temperature (LT) phase reaches $3.19 \text{ cm}^3 \text{ K mol}^{-1}$. Conversely, as the sample in the LT phase is warmed at a heating rate of 0.5 K min^{-1} , the $\chi_M T$ value suddenly increases near 285 K and reaches the HT phase value at 325 K. The transition temperatures from HT to LT ($T_{1/2\downarrow}$) and from LT to HT ($T_{1/2\uparrow}$) are 225 and 300 K, respectively, and the width of the thermal hysteresis loop ($\Delta T = T_{1/2\uparrow} - T_{1/2\downarrow}$) is 75 K. This temperature-induced phase transition is repeatedly observed [55, 56].

1.4.2 Change in Electronic State

X-ray photoelectron spectroscopy (XPS) spectra of $\text{K}^{\text{I}}_3[\text{Fe}^{\text{III}}(\text{CN})_6]$, $\text{K}^{\text{I}}_4[\text{Fe}^{\text{II}}(\text{CN})_6]$ and the HT and LT phases were measured. In the HT phase, the Fe- $2\text{P}_{3/2}$ and Mn- $2\text{P}_{3/2}$ electron binding energies are 710.1 and 641.8 eV, respectively, and in the LT phase, the Fe- $2\text{P}_{3/2}$ and Mn- $2\text{P}_{3/2}$ electron binding energies are 708.8 and 642.5 eV, respectively. The observed Fe- $2\text{P}_{3/2}$ electron binding energy of 710.1 eV in the HT phase corresponds to that of

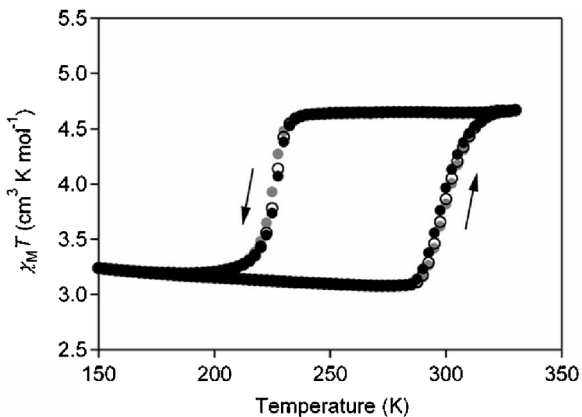


Fig. 1.3. The observed $\chi_M T - T$ plots under 5000 Oe with the first measurement (black circles), second measurement (white circles), and third measurement (gray circles). The down and up arrows indicate cooling and warming processes, respectively

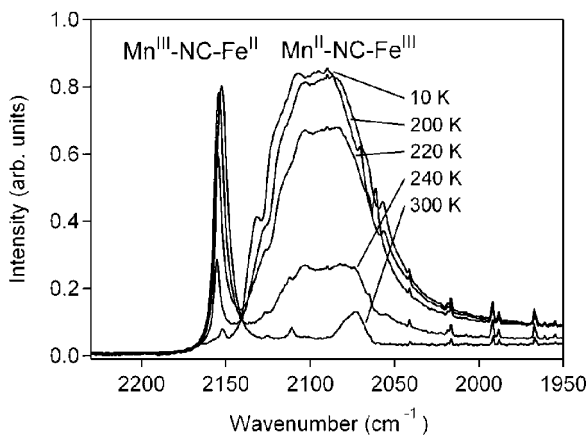


Fig. 1.4. Temperature dependence of the CN stretching frequencies in the IR spectra with cooling process

710.0 eV for Fe^{III} in $\text{K}^{\text{I}}_3[\text{Fe}^{\text{III}}(\text{CN})_6]$. In contrast, $\text{Fe-}2\text{P}_{3/2}$ binding energy of 708.8 eV in the LT phase is close to that of 709.1 eV for Fe^{II} in $\text{K}^{\text{I}}_4[\text{Fe}^{\text{II}}(\text{CN})_6]$. The shift of the $\text{Mn-}2\text{P}_{3/2}$ binding energy from the HT to the LT phases suggests that the oxidation number of the Mn ion increases from II to III.

Between 300 and 10 K, the infrared (IR) spectra are recorded. Figure 1.4 shows the CN^- stretching frequencies at 300, 240, 220, 200, and 10 K. At 300 K, a sharp CN^- peak is observed at 2152 cm^{-1} (linewidth = 9 cm^{-1}) and as the temperature decreases, the intensity of this peak decreases. Near 220 K a new broad peak appears at 2095 cm^{-1} (linewidth = 65 cm^{-1}). These IR changes are in the same temperature range of the phase transition in the $\chi_M T - T$ plots. The CN stretching peak at 2152 cm^{-1} in the HT phase is due

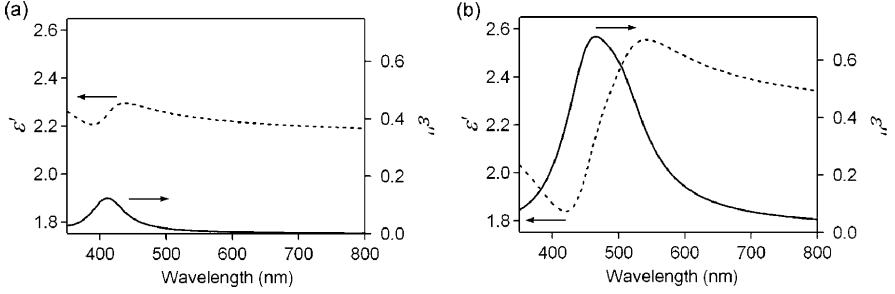


Fig. 1.5. Real (ϵ') and imaginary (ϵ'') parts of the dielectric constant (ϵ) spectra in the (a) HT phase and (b) LT phase. *Gray and black lines* represent the ϵ' and ϵ'' parts, respectively

to the CN ligand bridged to Mn^{II} and Fe^{III} ions ($\text{Mn}^{\text{II}}\text{-NC-Fe}^{\text{III}}$). In contrast, the broad CN stretching peak at 2095 cm^{-1} in the LT phase is assigned to the CN ligand bridged to Mn^{III} and Fe^{II} ions ($\text{Mn}^{\text{III}}\text{-NC-Fe}^{\text{II}}$).

These XPS and IR spectra show that valence states for Mn and Fe ions in the HT phase are $\text{Mn}^{\text{II}}(d^5)$ and $\text{Fe}^{\text{III}}(d^5)$, respectively, and those in the LT phase are $\text{Mn}^{\text{III}}(d^4)$ and $\text{Fe}^{\text{II}}(d^6)$, respectively. The drop in the $\chi_{\text{M}}T$ value at $T_{1/2\downarrow}$ implies that the electronic states of the HT and LT phases are $\text{Mn}^{\text{II}}(d^5; S = 5/2)\text{-NC-Fe}^{\text{III}}(d^5; S = 1/2)$ and $\text{Mn}^{\text{III}}(d^4; S = 2)\text{-NC-Fe}^{\text{II}}(d^6; S = 0)$, respectively. These assignments are confirmed by Mn and Fe 3p-1s X-ray emission spectroscopy [57] and 1s X-ray absorption spectroscopy [58].

Figure 1.5a shows the real (ϵ') and imaginary (ϵ'') parts of the dielectric constant (ϵ) spectrum of the HT phase at 293 K, measured by spectroscopic ellipsometry [59]. A dispersive-shaped line, which was centered at 410 nm, was observed. In the corresponding position, an absorption-shaped peak was observed in the ϵ'' spectrum at 410 nm with $\epsilon'' = 0.13$. This peak is assigned to the ligand-to-metal charge transfer (LMCT) transition of $[\text{Fe}(\text{CN})_6]^{3-} (^2\text{T}_{2\text{g}} \rightarrow ^2\text{T}_{1\text{u}}, \text{CN}^- \rightarrow \text{Fe}^{\text{III}})$. Figure 1.5b shows the ϵ' and ϵ'' parts of the ϵ spectrum in the LT phase. The LT phase was obtained by slowly cooling to 160 K using N_2 vapor, and then measuring ϵ at 275 K. A large dispersive-shaped line, which was centered at 470 nm with a minimum value at 420 nm and a maximum at 540 nm, was observed in the ϵ' spectrum. The corresponding position in the ϵ'' spectrum showed a strong absorption-shaped peak of $\epsilon'' = 0.68$, which is assigned to the metal-to-metal charge transfer (MMCT) band of $\text{Fe}^{\text{II}} \rightarrow \text{Mn}^{\text{III}}$ (more accurately, $\text{CN}_{2\text{px}}, \text{CN}_{2\text{py}} \rightarrow \text{Mn}_{3\text{dx}^2-y^2}, \text{Mn}_{3\text{dz}^2}$).

1.4.3 Structural Change

Figure 1.6 shows the powder X-ray diffraction (XRD) patterns as the temperature decreased from 300, 240, 220 to 160 K. The diffraction pattern of the HT phase is consistent with a face-centered cubic ($\text{F}\bar{4}3\text{m}$) structure with a lattice constant of 10.533 \AA (at 300 K). As the sample is cooled, the XRD

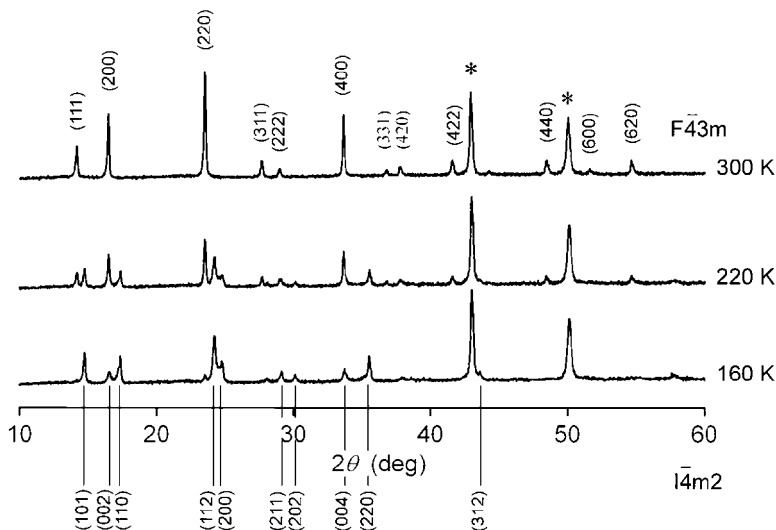


Fig. 1.6. Temperature dependences of XRD spectra (* indicates Cu from the sample holder)

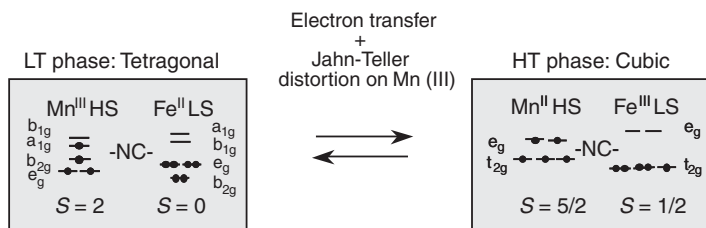


Fig. 1.7. Electronic states of the LT and HT phases

peaks of the HT phase decrease and different peaks appear. The observed XRD pattern in the LT phase shows a tetragonal structure of $I4m2$ with $a = b = 7.090$ Å and $c = 10.520$ Å (at 160 K), which corresponds to $a = b = 10.026$ Å and $c = 10.520$ Å in a cubic lattice. The unit cell volume of 1169 Å³ in the HT phase is reduced about 10% to $11,057$ Å³ in the LT phase and warming caused the tetragonal structure to return to the cubic one. This structural change from cubic to tetragonal in the XRD measurement is understood by the Mn^{III} Jahn–Teller transformation of the tetragonally octahedral elongation-type (B_{1g} oscillator mode). Synchrotron radiation X-ray powder structural analysis was used to determine the precise bond lengths of the LT phase, i.e., two-long and four-short Mn–N bond distances are $2.26(2)$ and $1.89(3)$ Å, respectively, and the two-short and four-long Fe–C bond distances are $1.89(2)$ and $2.00(3)$, respectively [60]. Thus, the d -orbital symmetry of both metal ions in the LT phase is D_{4th} (a_{1g}, b_{1g}, b_{2g} , and e_g). Therefore, the precise electronic state of LT phase is Mn^{III}($e_g^2 b_{2g}^1 a_{1g}^1; S = 2$)–NC–Fe^{II}($b_{2g}^2 e_g^4; S = 0$) (Fig. 1.7).

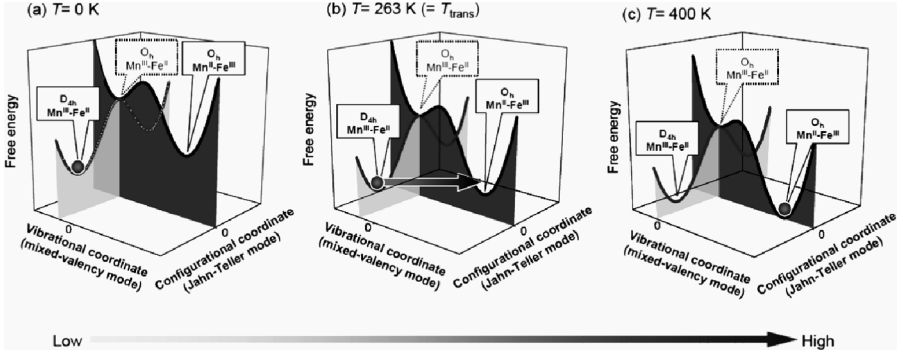


Fig. 1.8. The schematic free energy surfaces of this system in mixed-valence (*black curve*) and Jahn–Teller (*gray curve*) modes: (a) the ground state is $\text{Mn}^{\text{III}} - \text{Fe}^{\text{II}}$ and the meta-stable state is $\text{Mn}^{\text{II}} - \text{Fe}^{\text{III}}$ at $T = 0 \text{ K}$, (b) $T = 263 \text{ K} (=T_{\text{trans}})$, (c) the ground state is $\text{Mn}^{\text{II}} - \text{Fe}^{\text{III}}$ and meta-stable state is $\text{Mn}^{\text{III}} - \text{Fe}^{\text{II}}$ at $T = 400 \text{ K}$. Gray spheres indicate population

1.4.4 Mechanism

Prussian blue analogs belong to class II mixed-valence compounds. This system is described by two parabolic potential-energy curves due to valence isomers in the nuclear coordinates of the coupled vibrational mode [8–11]. When these two vibronic states interact, the ground state surface has two minima in the vibrational coordinates (Fig. 1.8). In the present system, the $\text{Mn}^{\text{III}} - \text{Fe}^{\text{II}}$ vibronic state is a ground state at $T = 0 \text{ K}$ in the vibrational coordinates (mixed-valency mode) (black curve in Fig. 1.8a). Moreover, in this situation, Mn^{III} causes Jahn–Teller distortion, and then the energy of the $\text{Mn}^{\text{III}} - \text{Fe}^{\text{II}}$ has two minima described in the configurational coordinates (Jahn–Teller mode) (gray curve in Fig. 1.8a). In the present system, Mn^{III} ion shows an elongation-type Jahn–Teller distortion. These potential surfaces change as the temperature increases, which cause a phase transition.

1.5 Ferromagnetism of the Low-Temperature Phase

1.5.1 Magnetic Ordering and Heat Capacity

When the LT phase is cooled to a very low temperature under an external magnetic field of 10 Oe, it exhibits spontaneous magnetization with a Curie temperature (T_c) of 11.3 K (Fig. 1.9a). The magnetization as a function of the external magnetic field at 3 K indicates that the saturated magnetization (M_s) value is $3.6 \mu_B$ and the coercive field (H_c) value is 1050 G (Fig. 1.9b). The $\chi_M^{-1} - T$ plots of the paramagnetic LT phase show positive Weiss temperatures (Θ) between 12 and 15 K, which are obtained by extrapolating the

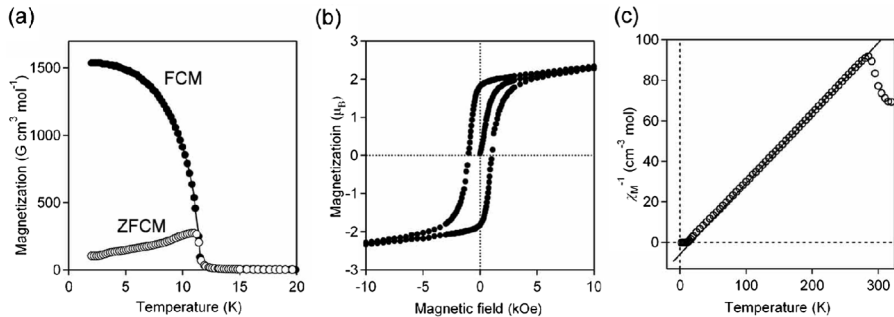


Fig. 1.9. (a) Magnetization vs. temperature plots of the LT phase by SQUID measurement: (●) Field-cooled magnetization (FCM) at 10 Oe, and (○) zero field-cooled magnetization (ZFCM) at 10 Oe. (b) Magnetic hysteresis loop of the LT phase at 3 K. (c) The observed $\chi_M - T$ plots. The data between 150 and 270 K is fitted to Curie-Weiss plots (—)

data in the temperature region of 150–270 K, respectively [61]. In low temperature region, the C_p value gradually increases with temperature and reaches a maximum, $27.1 \text{ J K}^{-1} \text{ mol}^{-1}$ at 11.0 K (denoted here as T_p), as shown in Fig. 1.10a. Then it drops suddenly to $17.5 \text{ J K}^{-1} \text{ mol}^{-1}$, and increases gradually. The dependence of the C_p values on the external magnetic field is shown in Fig. 1.10b and c, where the T_p peaks shift to a higher temperature as the external magnetic field increases: $T_p = 11.0 \text{ K}$ ($= 0 \text{ T}$), 11.0 K (0.05 T), 11.2 K (0.10 T), 11.3 K (0.20 T), 11.4 K (0.30 T), 11.5 K (0.50 T), 11.9 K (1.00 T), 13.8 K (2.00 T), and 15.2 K (3.00 T).

1.5.2 Entropy and Enthalpy of Magnetic Phase Transition

Because $\text{RbMn}[\text{Fe}(\text{CN})_6]$ is an insulating magnetic system, the C_p value is described as a sum of the contributions from lattice vibration, C_{lat} , short-range magnetic ordering, C_{short} , and long-range magnetic ordering, C_{long} :

$$C_p = C_{\text{lat}} + C_{\text{short}} + C_{\text{long}}. \quad (1.1)$$

C_{lat} is described by a polynomial function of temperature with odd powers [62],

$$C_{\text{lat}} = aT^3 + bT^5 + cT^7 + dT^9 + eT^{11} + \dots, \quad (1.2)$$

and C_{short} is described by AT^{-2} [63]. We fitted the C_p data in the region between 15 K ($= 1.4 \times T_c$) and 30 K ($= 2.7 \times T_c$) by the contributions of $C_{\text{lat}} + C_{\text{short}}$, using analyses reported in other systems [64]. The derived coefficients, including the estimated uncertainties ($\pm 7.4\%$) from the experiment ($\pm 7.0\%$) and curve fitting ($\pm 2.3\%$), are as follows: $a = 8.08 \times 10^{-3} \text{ J K}^{-4} \text{ mol}^{-1}$, $b = -2.10 \times 10^{-5} \text{ J K}^{-6} \text{ mol}^{-1}$, $c = 2.56 \times 10^{-8} \text{ J K}^{-8} \text{ mol}^{-1}$, $d = -1.18 \times 10^{-11} \text{ J K}^{-10} \text{ mol}^{-1}$, and $A = 1130 \text{ J K mol}^{-1}$. The

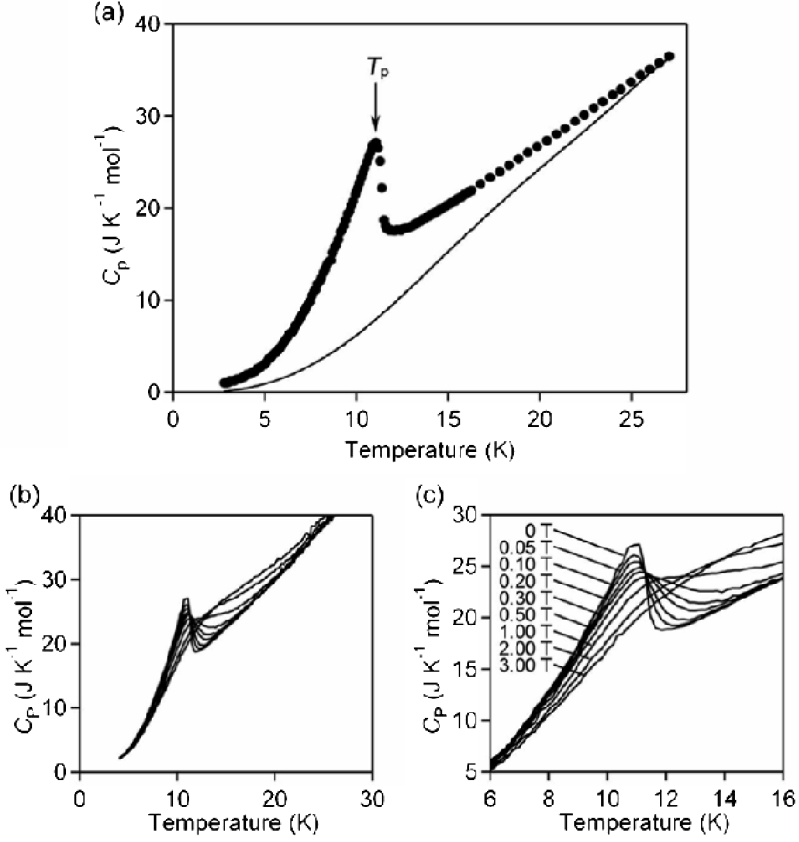


Fig. 1.10. (a) Plots of C_p vs. T in a zero external magnetic field: (●) experimental and (—) derived C_{lat} curve based on (1.3). (b) Plots of C_p vs. T in the presence of an external magnetic field. (c) Enlarged plots of (b)

solid line in Fig. 1.10a shows the C_{lat} curve. The magnetic heat capacity, $C_{\text{mag}} = C_{\text{short}} + C_{\text{long}}$, is obtained by subtracting C_{lat} from C_p , as shown in Fig. 1.11. The magnetic transition entropy, ΔS_{mag} , and enthalpy, ΔH_{mag} , can be obtained from

$$\Delta S_{\text{mag}} = \int_0^T C_{\text{mag}} d \ln T \quad (1.3)$$

and

$$\Delta H_{\text{mag}} = \int_0^T C_{\text{mag}} dT. \quad (1.4)$$

The estimated values of ΔS_{mag} and ΔH_{mag} for $\text{Rb}^{\text{I}}\text{Mn}^{\text{III}}[\text{Fe}^{\text{II}}(\text{CN})_6]$ are $11.8 \pm 0.9 \text{ J K}^{-1} \text{ mol}^{-1}$ and $125 \pm 9 \text{ J mol}^{-1}$, respectively.

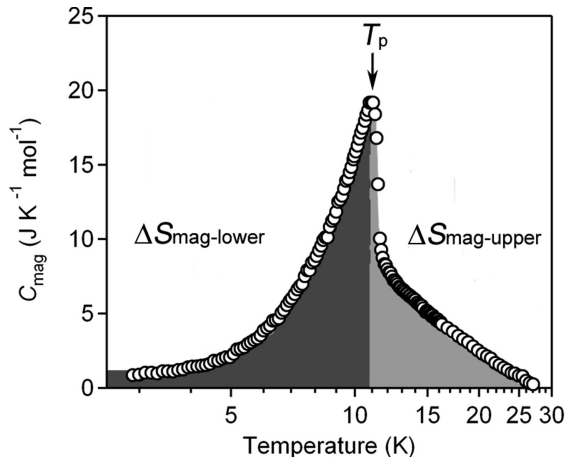


Fig. 1.11. Plots of C_{mag} vs. $\log T$

1.5.3 Long-Range Magnetic Ordering and Exchange Coupling

The T_p value of 11.0 K agrees with the T_C value of 11.3 K derived from a SQUID measurement, then, the anomalous peak at can be ascribed to a magnetic phase transition. The ΔS_{mag} value of $11.8 \pm 0.9 \text{ J K}^{-1} \text{ mol}^{-1}$ is close to the value calculated for the ordering of magnetic spins on the $\text{Mn}^{\text{III}} (S = 2)$ sites for $\text{Rb}^{\text{I}}\text{Mn}^{\text{III}}[\text{Fe}^{\text{II}}(\text{CN}_6)]$ given by $R \ln(2S+1) = 13.4 \text{ J K}^{-1} \text{ mol}^{-1}$, where R is the gas constant. Thus, the origin of this magnetic phase transition is attributed to the long-range magnetic ordering of the Mn^{III} sites.

The dimensionality of magnetic ordering, i.e., two- or three-dimensional (2- or 3-D) magnetic lattice, can be determined by the temperature dispersion of ΔS_{mag} . When the value of ΔS_{mag} is divided into two terms, such as the magnetic entropy values below T_p ($\Delta S_{\text{mag-lower}}$) and above T_p ($\Delta S_{\text{mag-upper}}$), the ratio of $\Delta S_{\text{mag-lower}} / \Delta S_{\text{mag}}$ for the magnetic lattices of the 3-D Ising, 2-D Ising, and 3-D Heisenberg types are 81, 44, and 62%, respectively [65]. The ratio of $\Delta S_{\text{mag-lower}} / \Delta S_{\text{mag}}$ in the present system is 65(3)% (Fig. 1.11). Therefore, in this framework the magnetic ordering of the LT phase is most likely 3-D Heisenberg-type magnetic ordering.

To analyzing C_{mag} at very low temperatures using the spin-wave theory can determine if the long-range magnetic ordering of a target material is ferromagnetic or antiferromagnetic. The heat capacity due to the spin-wave excitation, C_{SW} , is expressed by [66]:

$$C_{\text{SW}} = \alpha T^{\frac{d}{n}}, \quad (1.5)$$

where d stands for the dimensionality of the magnetic lattice and n is the exponent in the dispersion relationship: $n = 1$ for antiferromagnets and $n =$

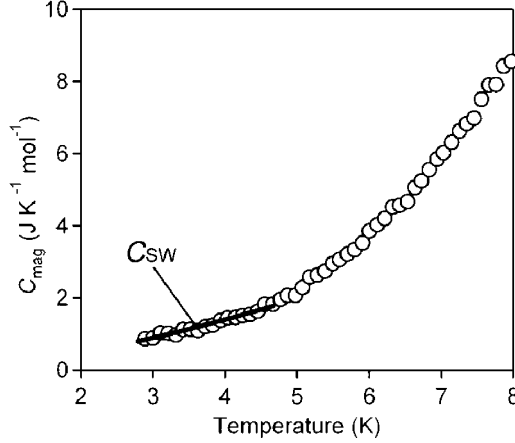


Fig. 1.12. Experimental plots of C_{mag} (\circ) and the C_{SW} curve ($-$) calculated from the spin-wave theory for a 3-D ferromagnet using (1.6) with $d/n = 1.51$ and $\alpha = 0.17 \text{ J K}^{-5/2} \text{ mol}^{-1}$

2 for ferromagnets. We fitted the C_{mag} values in the region between 2.8 and 4.7 K to (1.5) (Fig. 1.12) and the estimated parameter of d/n is 1.51(11). This d/n value is consistent with that predicted for the magnetic ordering of the LT phase, i.e., the 3-D ferromagnet, where $d = 3$ and $d = 2$. The observed shifts in the T_p values of the in-field C_p data, 11.0 K (0 T) \rightarrow 15.2 K (3.00 T) displayed in Fig. 1.10b and c, which also suggest ferromagnetic character. Since the shift in T_p to higher temperatures is characteristic of ferromagnetic transitions [67], the trend of the in-field C_p values observed in the present study gives direct evidence that the magnetic ordering of the LT phase is ferromagnetic.

This system shows a 3-D Heisenberg-type ferromagnetic ordering, although diamagnetic Fe^{II} is bridged to Mn^{III} in an alternating fashion. The exchange coupling constant, J , of this ferromagnet can be evaluated in the following manner. The α value derived from (1.5) is related to the J value. In C_{SW} for a 3-D ferromagnet, the coefficient α is described by [68]:

$$\alpha = \frac{1}{\sqrt{2}} \frac{5R\zeta(5/2)\Gamma(5/2)}{16\pi^2 S^{3/2}} \left(\frac{k_B}{J} \right)^{3/2}, \quad (1.6)$$

where ζ is Riemann's zeta function, Γ is Euler's gamma function, and k_B is the Boltzmann constant. Since the α value obtained from (1.5) is $0.17(1) \text{ J K}^{-5/2} \text{ mol}^{-1}$, the estimated J value based on (1.6) is $+0.55(4) \text{ cm}^{-1}$. ΔH_{mag} is also related to the J value in an extension of the molecular-field theory. In this treatment, ΔH_{mag} due to long-range magnetic ordering is expressed by

$$\frac{\Delta H_{\text{mag}}}{R} = \frac{S^2 z J}{k_B}, \quad (1.7)$$

where the number of neighboring magnetic sites, z , is 6 in the present system. The estimated J value from (1.7), using $\Delta H_{\text{mag}} = 125 \pm 9 \text{ Jmol}^{-1}$ is $+0.44(3) \text{ cm}^{-1}$.

1.5.4 Mechanism of Magnetic Ordering

Application of the superexchange interaction mechanism to the present ferromagnetic ordering is difficult since the diamagnetic Fe^{II} sites are connected by paramagnetic Mn^{III} sites. One plausible mechanism is the valence delocalization mechanism, in which ferromagnetic coupling arises from the charge-transfer configuration [69]. Day et al. explained the ferromagnetism of $\text{Fe}^{\text{III}}[\text{Fe}^{\text{II}}(\text{CN})_6]_{0.75} \cdot 3.5\text{H}_2\text{O}$ by the ferromagnetic exchange interaction based on a partial delocalization of the electrons that occupy the $\text{Fe}^{\text{II}}t_{2g}$ orbitals next to the neighboring high-spin Fe^{III} sites. Since Fe^{III} in Prussian blue is replaced with Mn^{III} , the same mechanism is feasible in our system. In fact, an intense intervalence transfer (IT) band of the LT phase has been observed at 540 nm and in the IT band of Prussian blue. In the valence delocalization mechanism, the T_c value is related to the valence delocalization coefficient of c as $T_c \propto c^4$. The c value is given by second-order perturbation theory as

$$c = \sum_{i=2,3} (\langle \psi_0 | H | \psi_i \rangle \langle \psi_1 | H | \psi_i \rangle / (E_1 - E_0)(E_i - E_0)), \quad (1.8)$$

where ψ_0, ψ_1, ψ_2 , and ψ_3 are the ground (pure $\text{Mn}^{\text{III}} - \text{Fe}^{\text{II}}$) state and the charge-transfer configurations of $\text{Fe}^{\text{II}} \rightarrow \text{Mn}^{\text{III}}$, $\text{Fe}^{\text{II}} \rightarrow \text{CN}$, and $\text{CN} \rightarrow \text{Mn}^{\text{III}}$, respectively, and $E_0 - E_3$ are their energies. Mixing these excited charge-transfer configurations with the ground state causes the ferromagnetic exchange coupling. The J value of $\approx +0.5 \text{ cm}^{-1}$ in the present system is three times larger than that of $+1.5 \text{ cm}^{-1}$ in Prussian blue. This large J value means that $\text{Rb}^{\text{I}}\text{Mn}^{\text{III}}[\text{Fe}^{\text{II}}(\text{CN})_6]$ has a large c value. Namely, the electrons on the Fe^{II} site are delocalized to the Mn^{III} site.

1.6 Control of Temperature-Induced Phase Transition

1.6.1 Huge Thermal Hysteresis Loop and a Hidden Stable Phase

$\text{Rb}_{0.64}\text{Mn}[\text{Fe}(\text{CN})_6]_{0.88} \cdot 1.7\text{H}_2\text{O}$ was prepared by reacting an aqueous solution (0.1 mol dm^{-3}) of MnCl_2 with a mixed aqueous solution of RbCl (1.0 mol dm^{-3}) and $\text{K}_3[\text{Fe}(\text{CN})_6]$ (0.1 mol dm^{-3}). The mixed solution was stirred for 5 min and the precipitate was filtered, yielding a light brown powder. The SEM image indicates that the precipitate is rectangular with the size of $0.3 \pm 0.1 \mu\text{m}$. The IR peak is observed at 2153 cm^{-1} at 300 K, which is assigned to the CN group of $\text{Fe}^{\text{III}} - \text{NC} - \text{Mn}^{\text{II}}$, i.e., the electronic state of the prepared compound is $\text{Rb}^{\text{I}}_{0.64}\text{Mn}^{\text{II}}[\text{Fe}^{\text{II}}(\text{CN})_6]_{0.88} \cdot 1.7\text{H}_2\text{O}$.

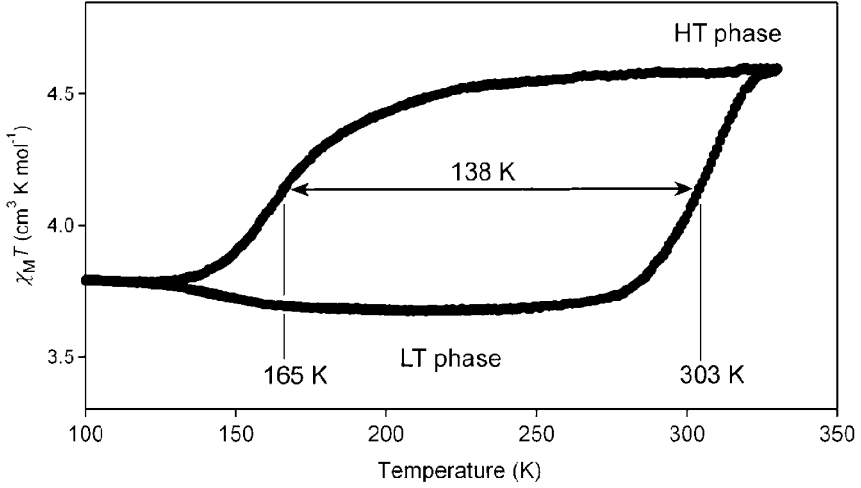


Fig. 1.13. The observed $\chi_M T$ vs. T plots for $\text{Rb}_{0.64}\text{Mn}[\text{Fe}(\text{CN})_6]_{0.88} \cdot 1.7\text{H}_2\text{O}$ under 5000 Oe with cooling and warming by $\pm 0.5 \text{ K min}^{-1}$

The magnetic properties were measured using a SQUID magnetometer. Figure 13 shows the product of the $\chi_M T$ vs. T plots. The $\chi_M T$ value decreases around 165 K ($= T_{1/2\downarrow}$) as the sample is cooled at a cooling rate of -0.5 K min^{-1} . Conversely, as the sample is warmed at a warming rate of $+0.5 \text{ K min}^{-1}$, the $\chi_M T$ value increases around 303 K ($= T_{1/2\uparrow}$) and returns to the initial value. The thermal hysteresis value ($\Delta T \equiv T_{1/2\uparrow} - T_{1/2\downarrow}$) is surprisingly large, 138 K. In addition, the χ_M value of the rapidly cooled sample, i.e., the sample placed directly into a sample chamber at 10 K, was measured. The rapidly cooled sample shows a high $\chi_M T$ value even at low temperature (hereafter called the hidden stable phase), which nearly corresponds to the value extrapolated from the HT phase, and then relaxes to the $\chi_M T$ value of low-temperature (LT) phase around 114 K ($= T_{\text{SP}\downarrow}$) (Fig. 1.14a). Since the χ_M^{-1} vs. T plots of the HT and LT phases are nearly linear as a function of T , these plots are fitted by the Curie-Weiss law and the Weiss temperatures of the HT and LT phases, which are estimated to be -6 K and $+7 \text{ K}$, respectively (Fig. 1.14b) [70].

To investigate the electronic state of the LT phase, the temperature dependence of the CN stretching frequencies in the IR spectrum was measured. As the temperature decreases, the intensity of the $\text{Mn}^{\text{II}} - \text{NC} - \text{Fe}^{\text{III}}$ peak at 2153 cm^{-1} decreases and a new broad peak appears between 2080 and 2140 (peak top: 2108 cm^{-1}), which is assigned to the CN group of $\text{Mn}^{\text{III}} - \text{NC} - \text{Fe}^{\text{II}}$. From the analysis of the conversion in the IR spectra, the electronic state of the LT phase is determined to be $\text{Rb}^{\text{I}}_{0.64}\text{Mn}^{\text{II}}_{0.40}\text{Mn}^{\text{III}}_{0.60}[\text{Fe}^{\text{II}}(\text{CN})_6]_{0.60}[\text{Fe}^{\text{III}}(\text{CN})_6]_{0.28} \cdot 1.7\text{H}_2\text{O}$. The XRD

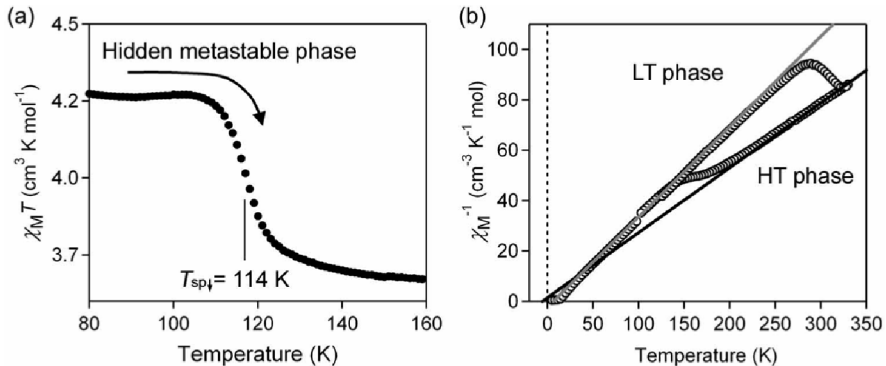


Fig. 1.14. (a) The observed $\chi_M T$ vs. T plots for $\text{Rb}_{0.64}\text{Mn}[\text{Fe}(\text{CN})_6]_{0.88} \cdot 1.7\text{H}_2\text{O}$ under 5000 Oe with warming by $+0.1 \text{ K min}^{-1}$ after rapid-cooling. (b) The observed χ_M^{-1} vs. T plots, and the χ_M^{-1} vs. T curves of the HT (black) and the LT (gray) phases, fitted by Curie-Weiss law

pattern of the sample at 300 K shows a cubic crystal ($\text{Fm}\bar{3}\text{m}$) with a lattice constant of $a = 10.535(6) \text{ \AA}$. As the temperature decreases, different XRD patterns due to the LT phase appear near $T_{1/2\downarrow}$. The observed XRD pattern in the LT phase is assigned to an orthorhombic crystal structure (F222) with lattice constants of $a = 10.261(16)$, $b = 10.044(10)$, and $c = 10.567(16) \text{ \AA}$. This distorted crystal structure is ascribed to the Jahn–Teller effect on the produced Mn^{III} sites.

1.6.2 Thermodynamical Analysis of Thermal Hysteresis Loop

The fractions (α) of the temperature-induced phase transition of $\Delta T = 138 \text{ K}$ are estimated as shown in Fig. 1.15a using the extrapolation curves of vs. χ_M^{-1} plots of the HT and LT phases. As a reference, χ_M^{-1} vs. T of $\text{RbMn}[\text{Fe}(\text{CN})_6]$ ($T_{1/2\downarrow} = 231 \text{ K}$, $T_{1/2\uparrow} = 304 \text{ K}$, and $\Delta T = 73 \text{ K}$) from our previous work [55] is also shown in Fig. 1.15b. These thermal hysteresis loops are analyzed based on SD model [71]. The Gibbs free energy G of the system is described by $G = \alpha\Delta H + \gamma\alpha(1 - \alpha) + T\{R[\alpha\ln\alpha + (1 - \alpha)\ln(1 - \alpha)] - \alpha\Delta S\}$, taking G of the LT phase as the origin of the energies, where α is the fraction of the HT phase, ΔH is the transition enthalpy, ΔS is the transition entropy, R is the gas constant, and the γ is an interaction parameter as a function of temperature, $\gamma = \gamma_a + \gamma_b T$ [71, 72]. Experimental heat capacity measurements indicate that the ΔH and ΔS values of $\text{RbMn}[\text{Fe}(\text{CN})_6]$ are $\Delta H = 1.7 \text{ kJ mol}^{-1}$ and $\Delta S = 6.0 \text{ J K}^{-1}$, respectively [55, 56]. When these thermodynamic parameters are used, the thermal hysteresis loops of $\text{Rb}_{0.64}\text{Mn}[\text{Fe}(\text{CN})_6]_{0.88} \cdot 1.7\text{H}_2\text{O}$ and $\text{RbMn}[\text{Fe}(\text{CN})_6]$ are well reproduced with the parameters of $(\Delta H, \Delta S, \gamma_a, \gamma_b) = (1.24 \text{ kJ mol}^{-1}, 4.54 \text{ J K}^{-1} \text{ mol}^{-1}, 20.1 \text{ kJ mol}^{-1}, 12.0 \text{ J K}^{-1} \text{ mol}^{-1})$ and $(\Delta H, \Delta S, \gamma_a, \gamma_b) = (1.68 \text{ kJ}$

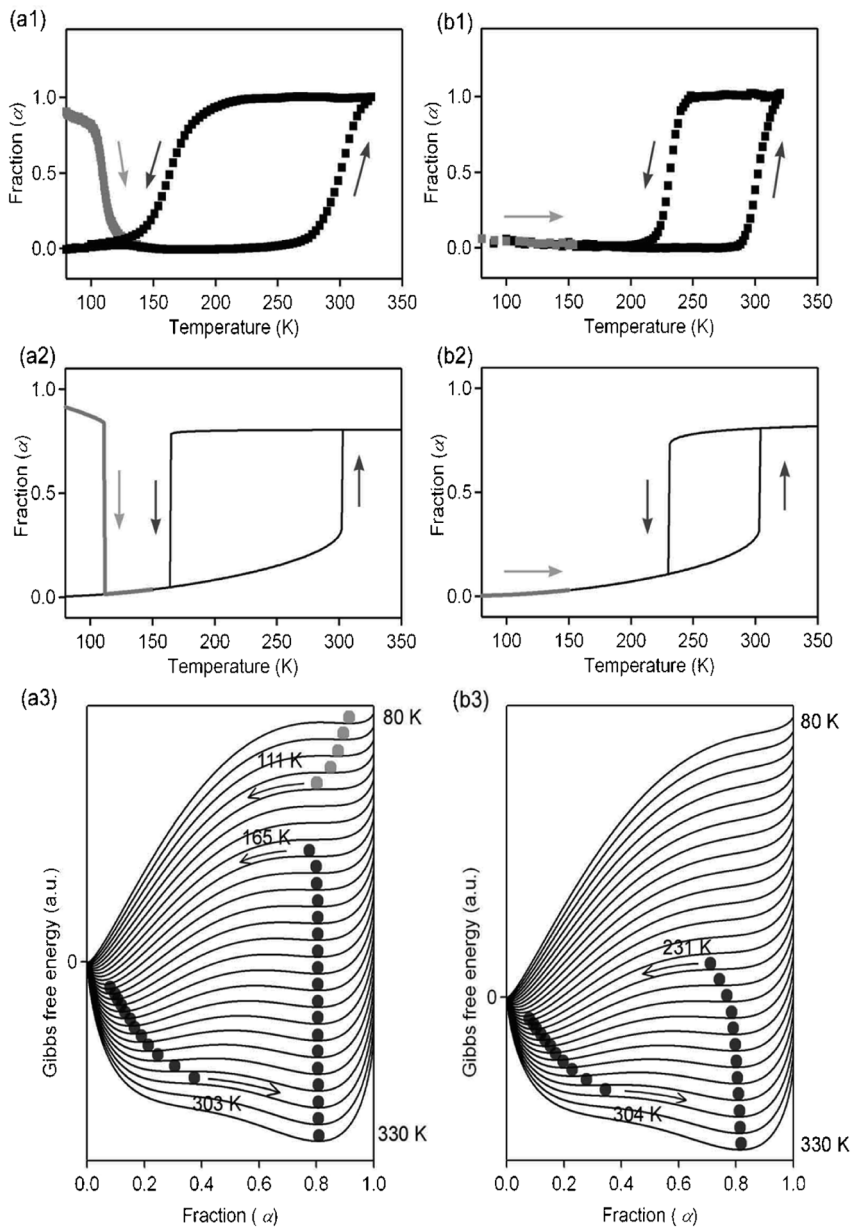


Fig. 1.15. The observed α vs. T plots of **(a1)** $\text{Rb}_{0.64}\text{Mn}[\text{Fe}(\text{CN})_6]_{0.88} \cdot 1.7\text{H}_2\text{O}$ and **(b1)** $\text{RbMn}[\text{Fe}(\text{CN})_6]$ from [55] where the *gray circles* show the rapidly-cooled sample upon warming. Calculated thermal hysteresis loops of **(a2)** $\text{Rb}_{0.64}\text{Mn}[\text{Fe}(\text{CN})_6]_{0.88} \cdot 1.7\text{H}_2\text{O}$ and **(b2)** $\text{RbMn}[\text{Fe}(\text{CN})_6]$. Temperature dependence of calculated vs. curves between 80 and 330 K with 10 K interval for **(a3)** $\text{Rb}_{0.64}\text{Mn}[\text{Fe}(\text{CN})_6]_{0.88} \cdot 1.7\text{H}_2\text{O}$ and **(b3)** $\text{RbMn}[\text{Fe}(\text{CN})_6]$. The *circles* indicate the thermal populations. The *black and gray circles* indicate the temperature-induced phase transition and the relaxation, respectively

mol^{-1} , $6.0 \text{ J K}^{-1} \text{ mol}^{-1}$, 20.5 kJ mol^{-1} , $11.9 \text{ J K}^{-1} \text{ mol}^{-1}$), respectively (Figs. 1.15(a2),(a3), black lines). In addition, $\text{Rb}_{0.64}\text{Mn}[\text{Fe}(\text{CN})_6]_{0.88} \cdot 1.7\text{H}_2\text{O}$ shows that a hidden stable phase exists at low temperature under thermal equilibrium condition (Fig. 1.15(a2), gray line). In this low temperature region, a local energy minimum exists at $\alpha = 0.85 - 0.9$ and relaxes to LT phase at 111 K (Fig. 1.15(a3), gray circles), which well reproduces the experimental data (Fig. 1.15(a1), gray circles). In contrast, both the calculated and experimental data of $\text{RbMn}[\text{Fe}(\text{CN})_6]$ indicate that this hidden stable phase does not exist (Fig. 1.15b). These results suggest that the observed phase in $\text{Rb}_{0.64}\text{Mn}[\text{Fe}(\text{CN})_6]_{0.88} \cdot 1.7\text{H}_2\text{O}$ is a hidden stable state of HT phase under thermal equilibrium condition and is not a supercooled phase under nonequilibrium condition. Furthermore, we calculated the α vs. T plots with various parameters, and thus, concluded that only the system showing a large thermal hysteresis loop produces the hidden stable phase under thermal equilibrium condition.

1.7 Photo-Induced Phase Collapse

1.7.1 Non Phase Transition Material

$\text{Rb}_{0.43}\text{Mn}[\text{Fe}(\text{CN})_6]_{0.81} \cdot 3\text{H}_2\text{O}$ was prepared by reacting an aqueous solution (0.1 mol dm^{-3}) of MnCl_2 with a mixed aqueous solution of RbCl (0.05 mol dm^{-3}) and $\text{K}_3[\text{Fe}(\text{CN})_6]$ (0.1 mol dm^{-3}). The temperature dependence of the magnetic susceptibility of the initial $\text{Mn}^{\text{II}} - \text{Fe}^{\text{III}}$ phase was measured using a SQUID magnetometer, and Fig. 1.16 plots the product of the $\chi_M T$ vs. T at a very slow cooling rate of -0.05 K min^{-1} . In the $\chi_M T - T$ plots, $\chi_M T$ remained nearly constant, corresponding to the sum of $\text{Mn}^{\text{II}} (S = 5/2)$ and $\text{Fe}^{\text{III}} (S = 1/2)$. Variable temperature IR spectra also showed that the CN stretching frequency peak due to $\text{Mn}^{\text{II}} - \text{NC} - \text{Fe}^{\text{III}}$ is maintained down to low temperature. The

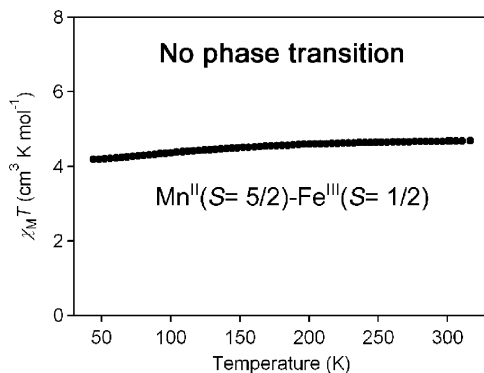


Fig. 1.16. The observed $\chi_M T$ vs. T plots for $\text{Rb}_{0.43}\text{Mn}[\text{Fe}(\text{CN})_6]_{0.81} \cdot 3\text{H}_2\text{O}$ under 5000 Oe

XRD pattern at 300 K confirmed that the crystal structure is face-centered cubic (space group: $Fm\bar{3}m$) with a lattice constant of $a = 10.473(9)\text{\AA}$. In the temperature range between 300 and 20 K, the lattice constant was almost constant, i.e., $a = 10.493(9)\text{\AA}$ at 20 K. These results indicate that a temperature-induced charge-transfer phase transition does not occur in the present material [73]. In spectroscopic ellipsometry, an optical resonance due to the ligand-to-metal charge transfer (LMCT) transition on $[\text{Fe}(\text{CN})_6]^{3-}$ was observed at 410 nm.

1.7.2 Photo-Induced Structural Transition

Since $\text{Rb}^{\text{I}}_{0.43}\text{Mn}^{\text{II}}[\text{Fe}^{\text{III}}(\text{CN})_6]_{0.81} \cdot 3\text{H}_2\text{O}$ has absorption at 410 nm, we irradiated the sample in XRD equipment with blue light ($410 \pm 25\text{ nm}$, 20 mW cm^{-2}) using a filtered Xe lamp. Upon blue-light irradiation, the XRD peaks of the $\text{Mn}^{\text{II}} - \text{Fe}^{\text{III}}$ phase decreased, and new XRD peaks appeared as shown in Fig. 1.17. The new XRD pattern of the PG phase was assigned to a face-centered cubic structure of $Fm\bar{3}m$ with $a = 10.099(3)\text{\AA}$. When the XRD pattern due to the PG phase was cooled to 20 K and then warmed above room temperature, it was maintained over a wide temperature range, but at 310 K the XRD pattern was perfectly restored to the original XRD pattern of the initial $\text{Mn}^{\text{II}} - \text{Fe}^{\text{III}}$ phase (Fig. 1.18a). The photo-conversion efficiency depended on the irradiation temperature as shown in Fig. 1.18b, i.e., 0% (20 K), 45% (100 K), 66% (140 K), 3% (180 K), 6% (220 K), and 0% (300 K) by blue light. To investigate the electronic state of the PG phase, the IR spectra after light

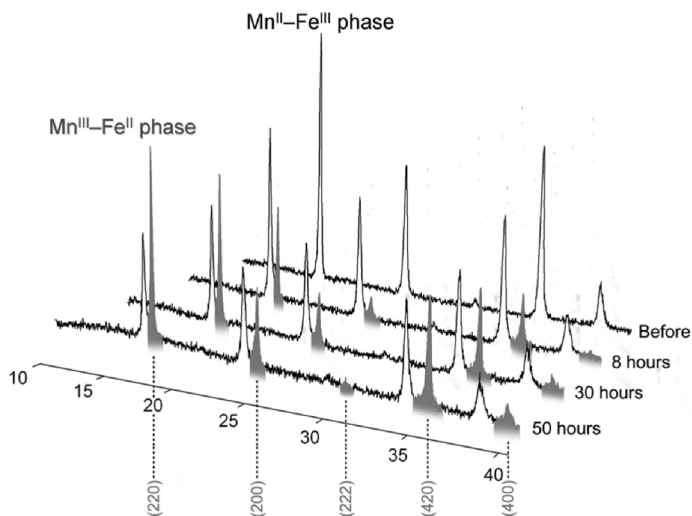


Fig. 1.17. Photo-induced phase collapse in $\text{Rb}_{0.43}\text{Mn}[\text{Fe}(\text{CN})_6]_{0.81} \cdot 3\text{H}_2\text{O}$ by blue-light irradiation. XRD patterns at 140 K before and after blue-light irradiation

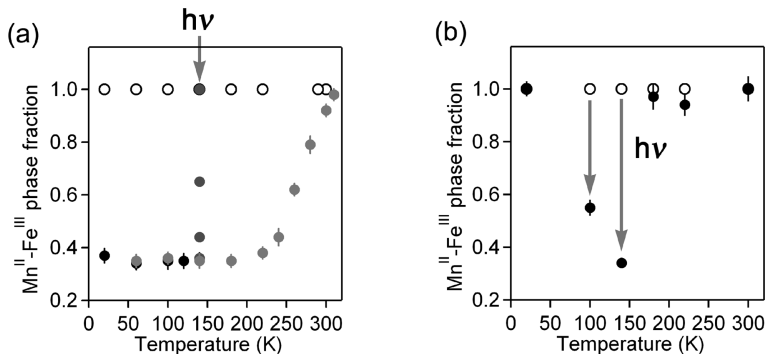


Fig. 1.18. (a) Temperature dependence of the Mn^{II} – Fe^{III} phase fraction before irradiation (*open circles*), during light irradiation at 140 K (*dark gray circles*), cooling process after irradiation (140 K → 20 K) (*black circles*), and warming process (20 K → 310 K) (*gray circles*). (b) Irradiation temperature dependence of the Mn^{II} – Fe^{III} phase fraction before (*open circles*) and after (*black circles*) light irradiation for 50 h (20 mW cm⁻²)

irradiation were measured at 140 K. Upon irradiation, the Mn^{II} – NC – Fe^{III} peak at 2153 cm⁻¹ decreased and a broad peak appeared at 2095 cm⁻¹, which corresponds to the CN stretching frequency of Mn^{III} – NC – Fe^{II}. Hence, the observed photo-induced phase collapse is caused by the charge-transfer phase transition from the Mn^{II} – Fe^{III} phase to the Mn^{III} – Fe^{II} phase.

1.7.3 Photo-Induced Phase Transition from a Metastable Phase to a Hidden Stable Phase

To understand the mechanism of the observed photo-induced phase transition, we calculated the Gibbs free energy vs. the Mn^{II} – Fe^{III} fraction for Rb_{0.43}Mn[Fe(CN)₆]_{0.81} · 3H₂O using the Slichter and Drickamer mean-field model [71], described by $G = \alpha\Delta H + \gamma\alpha(1 - \alpha) + T\{R[\alpha\ln\alpha + (1 - \alpha)\ln(1 - \alpha)] - \alpha\Delta S\}$, mentioned in Sect. 1.6.2. The thermodynamical parameters for the calculation were estimated by extrapolating our previous data. In the entire temperature range, a free-energy barrier existed between the mainly Mn^{II} – Fe^{III} phase and the mainly Mn^{III} – Fe^{II} phase, as shown in Fig. 1.19a. Since the material synthesis was carried out at room temperature and produced the Mn^{II} – Fe^{III} phase, the Mn^{II} – Fe^{III} phase is expected to be maintained in the entire temperature range as shown in Fig. 1.19a (dark gray circles). This calculation well explains the observed temperature dependence in Rb_{0.43}Mn[Fe(CN)₆]_{0.81} · 3H₂O, which does not exhibit a thermal phase transition. At the same time, this calculation predicts the existence of a hidden stable phase, the Mn^{III} – Fe^{II} phase (Fig. 1.19a, light gray circles). Its calculated temperature dependence (Fig. 1.19b, lower, light gray curve) corresponds well to the observed temperature dependence in Fig. 1.18a.

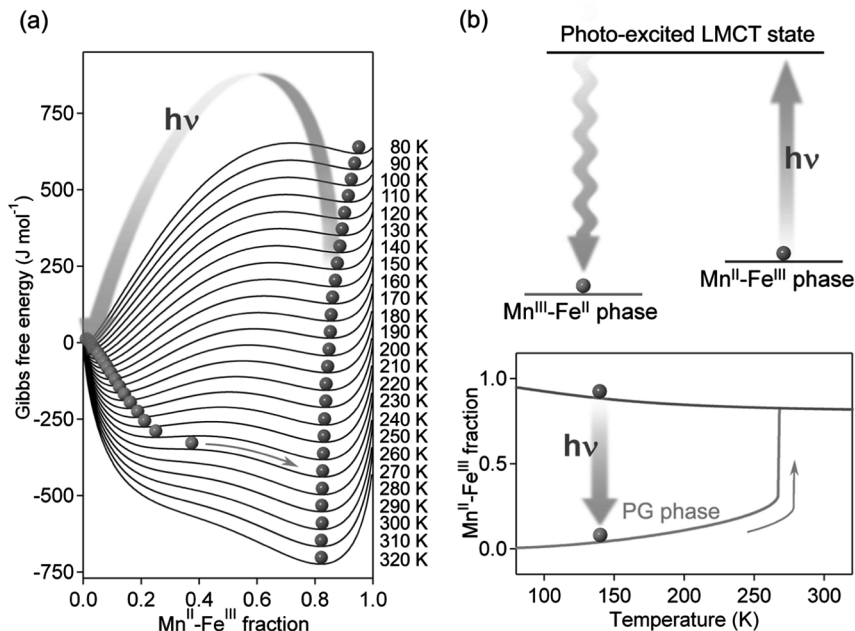


Fig. 1.19. Mechanism of the photo-induced phase collapse in $\text{Rb}_{0.43}\text{Mn}[\text{Fe}(\text{CN})_6]_{0.81} \cdot 3\text{H}_2\text{O}$. (a) Temperature dependence of calculated Gibbs free energy vs. the $\text{Mn}^{\text{II}} - \text{Fe}^{\text{III}}$ fraction for $\text{Rb}_{0.43}\text{Mn}[\text{Fe}(\text{CN})_6]_{0.81} \cdot 3\text{H}_2\text{O}$ based on the Slichter and Drickamer model. *Dark and light gray circles* indicate the existing populations of $\text{Mn}^{\text{II}} - \text{Fe}^{\text{III}}$ phase and $\text{Mn}^{\text{III}} - \text{Fe}^{\text{II}}$ phase, respectively. (b) Schematic picture of the pathway in the photo-induced phase collapse (*upper*). Temperature dependence of calculated fractions of $\text{Mn}^{\text{II}} - \text{Fe}^{\text{III}}$ mainly phase (*dark gray curve*) and $\text{Mn}^{\text{III}} - \text{Fe}^{\text{II}}$ mainly phase (*light gray curve*) (*lower*)

We thus conclude that the present photo-induced phase collapse is caused by a phase transition from a thermodynamically metastable $\text{Mn}^{\text{II}} - \text{Fe}^{\text{III}}$ phase to a $\text{Mn}^{\text{III}} - \text{Fe}^{\text{II}}$ true stable phase though the excited state of LMCT ($\text{CN}^- \rightarrow \text{Fe}^{\text{III}}$), which is excited by blue-light irradiation (Fig. 1.19b, upper).

1.8 Photo-Induced Phase Transition at Room Temperature

The photo-induced effect in the paramagnetic region was investigated with $\text{Rb}_{0.97}\text{Mn}[\text{Fe}(\text{CN})_6]_{0.99} \cdot 0.2\text{H}_2\text{O}$ using IR spectroscopy [74, 75]. A pulsed Nd^{3+} ; YAG laser ($\lambda = 532 \text{ nm}$; pulse width: 6 ns) was used. The $\chi_{\text{M}}T - T$ plots showed that $\text{Rb}_{0.97}\text{Mn}[\text{Fe}(\text{CN})_6]_{0.99} \cdot 0.2\text{H}_2\text{O}$ exhibited a temperature-induced phase transition (Fig. 1.20). The $T_{1/2\downarrow}$ and $T_{1/2\uparrow}$ were 220 and 314 K, respectively.

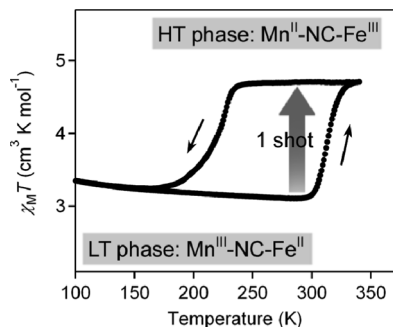


Fig. 1.20. The observed $\chi_M T - T$ plots for $\text{Rb}_{0.97}\text{Mn}[\text{Fe}(\text{CN})_6]_{0.99} \cdot 0.2\text{H}_2\text{O}$ in the cooling (\downarrow) and warming (\uparrow) processes under 5000 Oe

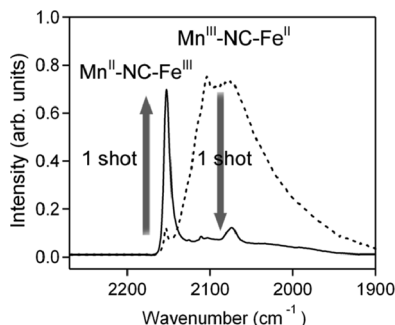


Fig. 1.21. Change in the IR spectrum by a one-shot-laser-pulse irradiation of 532 nm with $80 \text{ mJ cm}^{-2} \text{ pulse}^{-1}$ at 295 K for $\text{Rb}_{0.97}\text{Mn}[\text{Fe}(\text{CN})_6]_{0.99} \cdot 0.2\text{H}_2\text{O}$. The spectra before and after irradiation are shown as *dotted* and *solid* lines, respectively

Figure 1.21 shows the changes in the IR spectra before and after a one-shot-laser-pulse irradiation at 295 K, which is a temperature inside the thermal hysteresis loop. A one-shot-laser-pulse irradiation changed the IR spectrum of the LT phase to that of the HT phase. The IR spectrum of the irradiated sample returned to that of the initial LT phase by cooling ($295 \text{ K} \rightarrow 77 \text{ K} \rightarrow 295 \text{ K}$). Figure 1.22a shows the conversion fraction as a function of laser power density at 295, 280, 260, 240 and 220 K. The conversion fraction depended on the P value and temperature. A threshold in the laser power density (P_{th}) was observed. At 295 K, when the P value was greater than $6 \text{ mJ cm}^{-2} \text{ pulse}^{-1}$, the LT phase was converted to HT phase. In contrast, in the case of $P < P_{\text{th}}$, photo-conversion did not occur even after irradiating more than thousand shots. The existence of a threshold suggests that cooperative effects exist in the present photo-induced phase transition and the maximum value of quantum yield was $\Phi = 38$ at $P = 24 \text{ mJ cm}^{-2} \text{ pulse}^{-1}$ (Fig. 1.22b).

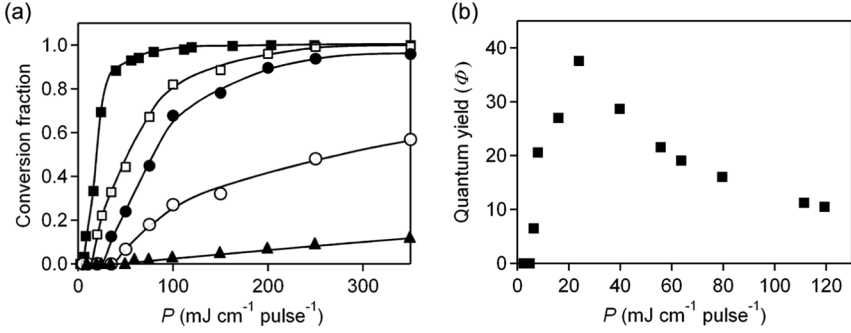


Fig. 1.22. (a) Laser power density (P) dependence of a one-shot-laser-pulse induced phase transition for $\text{Rb}_{0.97}\text{Mn}[\text{Fe}(\text{CN})_6]_{0.99} \cdot 0.2\text{H}_2\text{O}$ when irradiating with 532 nm at 295 (■), 280 (□), 260 (●), 240 (○) and 220 K (▲). *Solid line* is for the eye guide. (b) Laser power density (P) dependence of quantum yield Φ of a one-shot-laser-pulse induced phase transition at 295 K

In rubidium manganese hexacyanoferrate, temperature-induced phase transition is observed with large thermal hysteresis loops. The charge transfer from Mn^{II} to Fe^{III} accompanying the Jahn–Teller effect on the $\text{Mn}^{\text{III}}\text{N}_6$ moiety explains this phase transition. In paramagnetic state of this system, the photo-induced phase transition inside the thermal hysteresis loop was observed at room temperature. Such a photo-induced phase transition phenomena are caused by: (1) the change of valence states on transition metal ions due to a metal-to-metal charge-transfer and (2) the bistability due to the Jahn–Teller distortion of Mn^{III} ion.

1.9 Photomagnetism

1.9.1 Photo-Induced Demagnetization by One-Shot-Laser-Pulse

In this section, the photomagnetic effect of the LT phase was investigated with $\text{Rb}_{0.88}\text{Mn}[\text{Fe}(\text{CN})_6]_{0.96} \cdot 0.6\text{H}_2\text{O}$ using SQUID magnetometer [38, 76]. A pulsed Nd^{3+} ; YAG laser ($\lambda = 532$ nm; pulse width: 6 ns) was guided by optical fiber into the SQUID magnetometer. As $\text{Rb}_{0.88}\text{Mn}[\text{Fe}(\text{CN})_6]_{0.96} \cdot 0.6\text{H}_2\text{O}$ was cooled to a very low temperature under an external magnetic field of 10 Oe, the LT phase exhibited spontaneous magnetization with a T_c of 12 K. The M_s and H_c values at 2 K were $3.6 \mu_B$ and 1800 G, respectively. This M_s value can be explained by the ferromagnetic spin ordering of Mn^{III} ($S = 2$) ions. From the χ_M^{-1} vs. T plots at temperature between 100 and 250 K, the positive Weiss temperature value of +15 K was obtained.

When the sample was irradiated by one-shot-laser-pulse with 532 nm-laser light at 3 K, the magnetization was decreased. Figure 1.23a shows the magnetization vs. temperature curve for the sample irradiated with $P = 130 \text{ mJ cm}^{-2}$

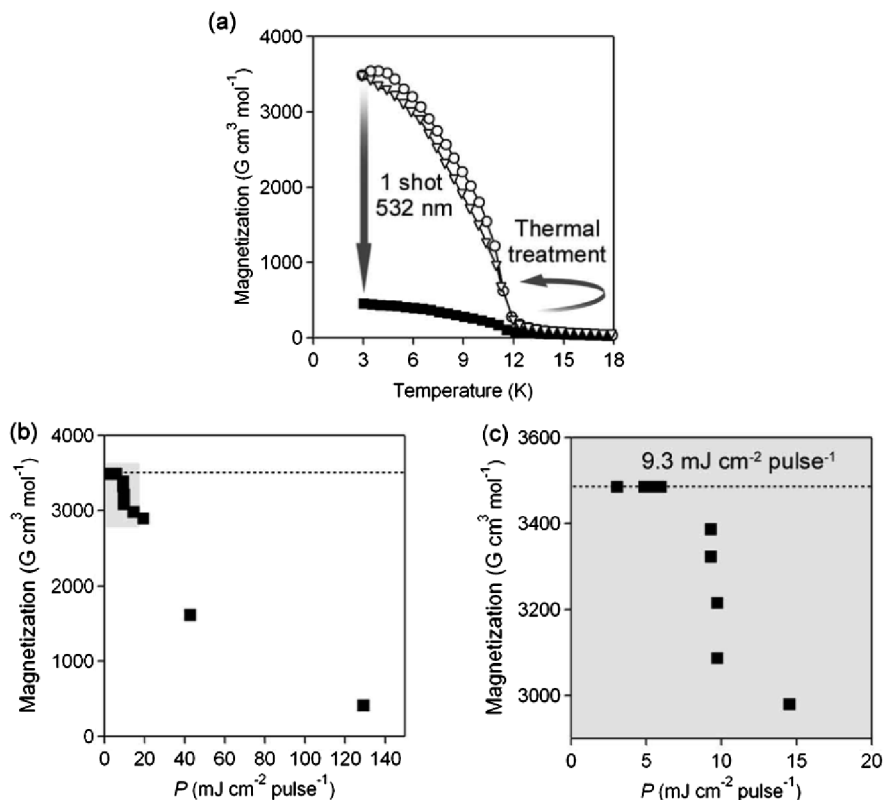


Fig. 1.23. (a) Magnetization vs. temperature plots for $\text{Rb}_{0.88}\text{Mn} [\text{Fe}(\text{CN})_6]_{0.96} \cdot 0.6\text{H}_2\text{O}$ at 200 Oe before (○) and after the one-shot-laser-pulse irradiation (■) and thermal treatment (▽). (b) Laser power density (P) dependences of the one-shot-laser-pulse induced photodemagnetization phenomenon. (c) Enlarged plots of (b)

pulse⁻¹. The photo-conversion increased with increasing the laser power density (P) as shown in Fig. 1.23b and c. A threshold in the laser power density (P'_{th}) was observed; when the P value was above $9.3 \text{ mJ cm}^{-2} \text{ pulse}^{-1}$, the magnetization value was decreased, however, in the case of $P < P'_{\text{th}}$, the magnetization value did not change. The quantum yields (Φ) for the present photodemagnetization were above one, e.g., $\Phi = 4.5$ ($= 43 \text{ mJ cm}^{-2} \text{ pulse}^{-1}$). The irradiated sample returned to the LT phase by an annealing treatment (3 K \rightarrow 150 K \rightarrow 3 K) with a relaxation at 120 K. The IR spectra before and after one-shot-laser-pulse irradiation (532 nm, $P = 14 \text{ mJ cm}^{-2} \text{ pulse}^{-1}$) at 8 K was obtained. After irradiation, the $\text{Mn}^{\text{III}} - \text{NC} - \text{Fe}^{\text{II}}$ peak at 2095 cm^{-1} disappears and a sharp peak due to the $\text{Mn}^{\text{II}} - \text{NC} - \text{Fe}^{\text{III}}$ peak at 2152 cm^{-1} appears. Note that, in the case of $P < P'_{\text{th}}$, the IR spectra were not changed by irradiation of several tens shots. An annealing treatment (8 K \rightarrow 150 K \rightarrow 8 K) returned the IR spectrum of the irradiated sample to the LT phase. From

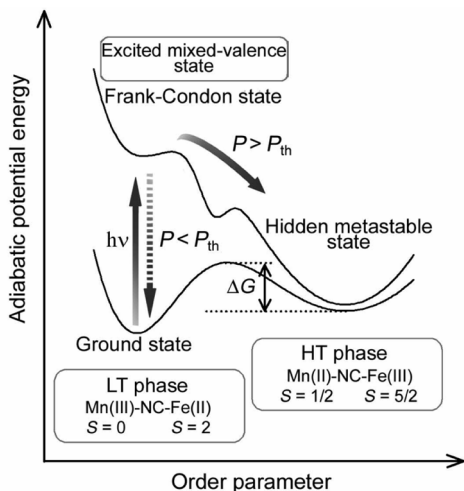


Fig. 1.24. Schematic illustration of the one-shot-laser-pulse-induced phase transition from the stable $\text{Mn}^{\text{III}} - \text{NC} - \text{Fe}^{\text{II}}$ phase to the hidden substable $\text{Mn}^{\text{II}} - \text{NC} - \text{Fe}^{\text{III}}$ phase

these results, we conclude that the present photo-demagnetization is caused by the photo-induced phase transition from the LT phase to the HT phase.

Temperature-induced phase transition between the LT and HT phases was observed in rubidium manganese hexacyanoferrate. In such a material with a bistability, a ground state can be converted to a hidden metastable state by the irradiation. Nasu et al. showed a simple scheme for a photo-induced phase transition using the adiabatic potential energy vs. order parameter (Fig. 1.24) [2]. In this scheme, the ground state is excited to the Franck–Condon state by irradiation. This Franck–Condon state proceeds to a hidden substable state through a structural change state or relaxes to the ground state. In our case, irradiating with pulsed-laser light excites the LT phase to a mixed-valence state between the $\text{Mn}^{\text{III}} - \text{Fe}^{\text{II}}$ and the $\text{Mn}^{\text{II}} - \text{NC} - \text{Fe}^{\text{III}}$ states. This mixed-valence state proceeds to the HT phase or relaxes to the initial LT phase. The produced HT phase can be maintained in the low temperature range since it is sufficiently separated from the LT phase by the thermal energy (ΔG). In addition, when the P value is larger than P_{th}' , the excited state proceeds to the photo-produced HT phase as shown by the solid arrow in Fig. 1.24. In contrast, when $P < P_{\text{th}}'$, the excited state relaxes to the ground state as shown by the dotted arrow.

1.9.2 Reversible Photomagnetic Effect

In previous section, we have reported that irradiating with 532 nm light converts the LT phase to the photo-induced (PI) phase, which decreases

its spontaneous magnetization. In this section, we have found that irradiating with a different wavelength of light recovers the PI phase in $\text{Rb}_{0.88}\text{Mn}[\text{Fe}(\text{CN})_6]_{0.96} \cdot 0.5\text{H}_2\text{O}$ to the LT phase. Furthermore, neutron powder diffraction using an analog complex, $\text{Rb}_{0.58}\text{Mn}[\text{Fe}(\text{CN})_6]_{0.86} \cdot 2.3\text{H}_2\text{O}$, has confirmed the magnetic ordering of the PI phase. Herein, we show the visible-light reversible changes in the electronic and magnetic properties of $\text{Rb}_{0.88}\text{Mn}[\text{Fe}(\text{CN})_6]_{0.96} \cdot 0.5\text{H}_2\text{O}$, the neutron powder diffraction pattern of $\text{Rb}_{0.58}\text{Mn}[\text{Fe}(\text{CN})_6]_{0.86} \cdot 2.3\text{H}_2\text{O}$, and the mechanism of the observed photo-reversible photomagnetism [77].

Photo-Reversible Changes in the IR Spectra and SQUID Measurement

Because a metal-to-metal charge transfer (MM'CT) band was observed at 420–540 nm in the ϵ spectrum of the LT phase (Fig. 1.5), the LT phase was irradiated with a CW diode green laser ($h\nu 1$; $\lambda = 532$ nm). Figure 1.25 shows the IR spectra before and after the light irradiations at 3 K. Before irradiating (Fig. 1.25a, black line), the LT phase possessed a broad peak due to $\text{Mn}^{\text{III}} - \text{NC} - \text{Fe}^{\text{II}}$ around 2100 cm^{-1} . Irradiating with $h\nu 1$ reduced the $\text{Mn}^{\text{III}} - \text{NC} - \text{Fe}^{\text{II}}$ peak, and created a sharp peak at 2153 cm^{-1} . The latter peak is assigned to the $\text{Mn}^{\text{II}} - \text{NC} - \text{Fe}^{\text{III}}$, which was also observed in the HT phase (2154 cm^{-1}). It is concluded that the PI phase after $h\nu 1$ irradiation has a valence state similar to the HT phase. Based on the knowledge that resonance due to the LMCT band was observed at 410 nm in the spectrum of the HT phase, this PI phase was irradiated with blue light ($h\nu 2$;

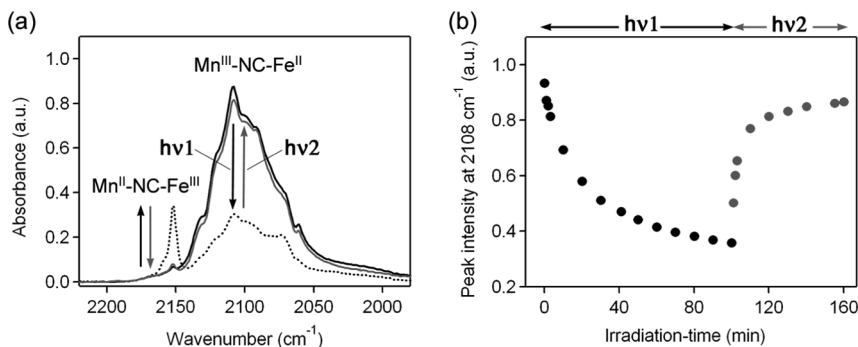


Fig. 1.25. Visible-light reversible change in the IR spectra of $\text{Rb}_{0.88}\text{Mn}[\text{Fe}(\text{CN})_6]_{0.96} \cdot 0.5\text{H}_2\text{O}$. (a) Changes in the IR spectrum at 3 K by irradiating with $h\nu 1$ ($\lambda = 532$ nm: *black arrows*) before irradiation (*black line*), after $h\nu 1$ irradiation (*dotted line*), and $h\nu 2$ irradiation (*gray line*). (b) Peak intensity at 2108 cm^{-1} vs. irradiation-time upon irradiating with $h\nu 1$ (*black circles*) and $h\nu 2$ (*gray circles*)

$\lambda = 410 \pm 30$ nm) from a filtered Xe lamp in order to investigate the photo-reversibility. Consequently, the $\text{Mn}^{\text{II}} - \text{NC} - \text{Fe}^{\text{III}}$ peak decreased and the $\text{Mn}^{\text{II}} - \text{NC} - \text{Fe}^{\text{III}}$ peak increased as shown in Fig. 1.25a. Figure 1.25b plots the peak intensities of $\text{Mn}^{\text{II}} - \text{NC} - \text{Fe}^{\text{III}}$ vs. irradiation-time. This photo-reversibility was repeatedly observed.

Next, we measured the photo-reversible change in magnetization *in situ* using SQUID equipment. The field cooled magnetization curve under an external magnetic field of 200 Oe showed that the LT phase is a ferromagnet with a T_c of 12 K (Fig. 1.26a, closed squares). Upon irradiating with $h\nu 1$ at 3 K, the magnetization value decreased from 5600 to 700 $\text{G cm}^3 \text{ mol}^{-1}$ (Fig. 1.26a, open circles).

Successively irradiating the PI phase with $h\nu 2$ increased the magnetization, which reached $4700 \text{ G cm}^3 \text{ mol}^{-1}$ (Fig. 1.26a, closed circles). The present photo-reversibility of the magnetization was repeatedly observed by alternately irradiating with $h\nu 1$ and $h\nu 2$ (Fig. 1.26b). The magnetization value after irradiating with $h\nu 2$, which is shown as the closed circles in Fig. 1.26a, was smaller than that of initial value, suggesting that a photo-equilibrium state persists. To confirm the photo-equilibrium behavior, we investigated the photo-effect of the reverse process, that is, from the PI phase to the LT phase, using a different light ($h\nu 3$; $\lambda = 425 \pm 45$ nm). Irradiating with $h\nu 3$ increased the magnetization, which reached plateau- $\text{Mag}_{h\nu 3}$ as shown in Fig. 1.27. Subsequent irradiation with $h\nu 2$ further increased the magnetization, which reached plateau- $\text{Mag}_{h\nu 2}$. This equilibrium behavior is due to a photo-stationary state between the photo-demagnetization (LT \rightarrow PI phase) and the photo-induced magnetization (PI \rightarrow LT phase).

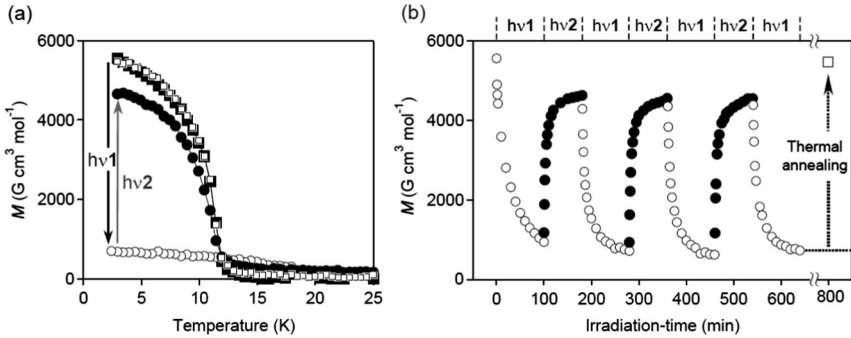


Fig. 1.26. Visible-light reversible photomagnetism in $\text{Rb}_{0.88}\text{Mn}[\text{Fe}(\text{CN})_6]_{0.96} \cdot 0.5\text{H}_2\text{O}$. (a) Magnetization vs. temperature curves at 200 Oe; before irradiating (\blacksquare), after $h\nu 1$ ($\lambda = 532$ nm, 30 mW cm^{-2}) irradiation for 100 min (\circ), after $h\nu 2$ ($\lambda = 410$ nm, 13 mW cm^{-2}) irradiation for 80 min (\bullet), and after the thermal annealing treatment of 180 K (\square). (b) Magnetization vs. irradiation-time plot at 3 K by alternating with $h\nu 1$ (\circ) and $h\nu 2$ (\bullet) light irradiation, and the magnetization value after a thermal treatment of 180 K (\square)

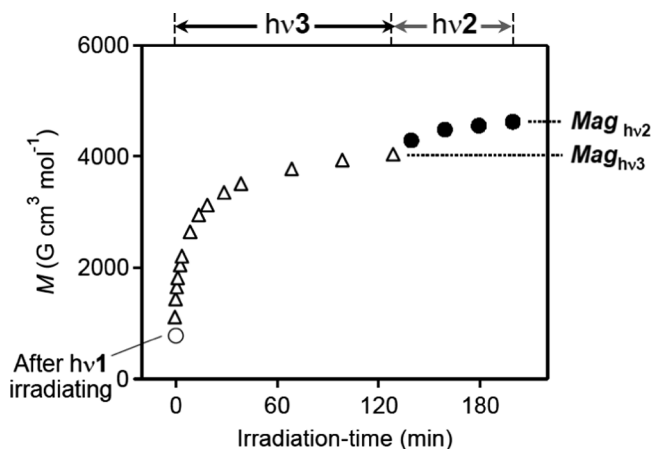


Fig. 1.27. Photo-stationary state between photodemagnetization and photo-induced magnetization. Magnetization vs. irradiation-time plot at 3 K upon irradiating with $h\nu 3$ ($\lambda = 425 \pm 445$ nm, 22 mW cm^{-2}) (open triangle) and then $h\nu 2$ ($\lambda = 410 \pm 30$ nm, 13 mW cm^{-2}) (black circles)

Magnetic Ordering of the Photo-Induced Phase

To determine the magnetic ordering of the PI phase, we performed neutron powder diffraction using an analog complex, $\text{Rb}_{0.58}\text{Mn}[\text{Fe}(\text{CN})_6]_{0.86} \cdot 2.3\text{H}_2\text{O}$. A charge-transfer phase transition was not observed in the IR spectrum of $\text{Rb}_{0.58}\text{Mn}[\text{Fe}(\text{CN})_6]_{0.86} \cdot 2.3\text{H}_2\text{O}$ when the sample was cooled to 3 K at a rate of -0.5 K (Fig. 1.28a). The $\chi_M^{-1} - T$ plot showed a negative Weiss temperature of -16 K, which was obtained by the least-square fitting in the temperature region of 150 - 320 K. The magnetization vs. temperature curve under an external field of 10 Oe exhibited an antiferromagnetic behavior with a Neel temperature (T_N) of 11.5 K. The magnetization vs. external magnetic field plots at 2 K showed a linear change (Fig. 1.28b). These magnetic data suggest that in $\text{Rb}_{0.58}\text{Mn}[\text{Fe}(\text{CN})_6]_{0.86} \cdot 2.3\text{H}_2\text{O}$, the HT phase is maintained even at low temperature and the HT phase shows antiferromagnetism. Figure 1.28c shows the neutron powder pattern for $\text{Rb}_{0.58}\text{Mn}[\text{Fe}(\text{CN})_6]_{0.86} \cdot 2.3\text{H}_2\text{O}$ at 30 K. Rietveld analysis showed that the crystal structure was tetragonal (P4/mmm) with lattice constants of $a = b = 7.424(6)$ Å and $c = 10.51(1)$ Å, which correspond to $a' = b' = 10.499$ Å and $c' = 10.51(1)$ Å in the frame of a cubic lattice. The interatomic distances of Fe and C in the ab plane ($\text{Fe} - \text{C}_{ab}$) and along the c axis ($\text{Fe} - \text{C}_c$) are 1.93(3) and 1.81(4) Å, respectively. The distances of $\text{Mn} - \text{N}_{ab}$ and $\text{Mn} - \text{N}_c$ are 2.18(2) and 2.18(4) Å, respectively.

Figure 1.29a and b shows the neutron powder diffraction patterns at 2 and 30 K, and the magnetic Bragg reflections as the difference in the patterns of 2 and 30 K, respectively. Analysis of the magnetic Bragg reflections suggests that this system is a layered antiferromagnet in which the magnetic coupling between the layers is antiferromagnetic. The spin arrangement as shown in

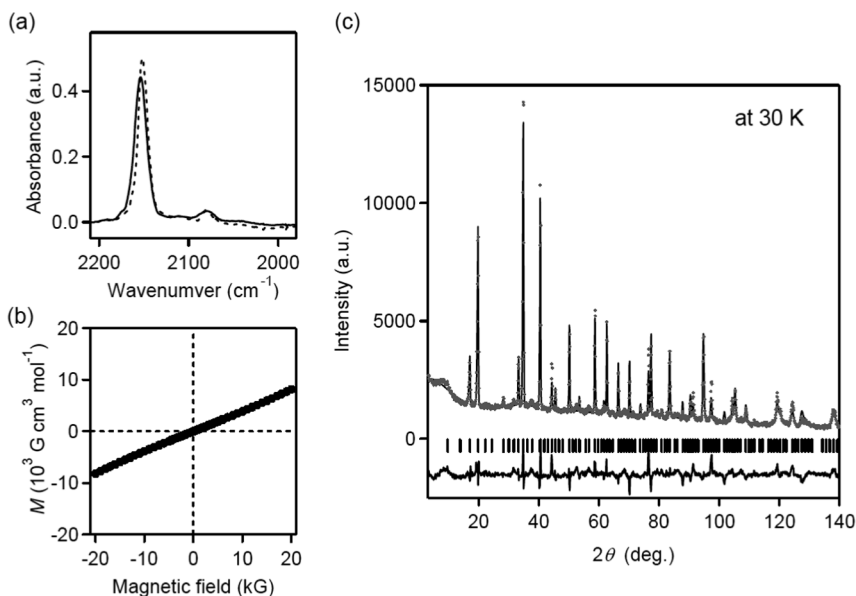


Fig. 1.28. Electronic state, magnetic property, and neutron powder diffraction pattern of $\text{Rb}_{0.58}\text{Mn}[\text{Fe}(\text{CN})_6]_{0.86} \cdot 2.3\text{H}_2\text{O}$. (a) IR spectra at 300 K (*dotted line*) and 3 K (*solid line*). (b) Magnetization as a function of the external magnetic field at 2 K. (c) Neutron powder diffraction pattern at 30 K. *Gray dots*, *black pattern*, and *black line* are the observed plots, calculated pattern, and their difference, respectively. *Bars* represent the calculated positions of the Bragg reflections

Fig. 1.29d is a suitable configuration due to the following reason. The electronic state of Mn^{II} is a $3d^5$ high-spin state and hence, all the $3d$ orbitals are magnetic orbitals. In contrast, Fe^{III} is a $3d^5$ low-spin state, and thus, only one of the t_{2g} orbitals becomes a magnetic orbital. Rietveld analysis showed elongation of $\text{Fe}(\text{CN})_6$ in the ab -plane, indicating that the d_{yz} and d_{zx} orbitals are more stabilized than the d_{xy} orbital due to backbonding of the cyanide ligand. Hence, the d_{xy} becomes the magnetic orbital of Fe^{III} . In this case, only the spin configuration shown in Fig. 1.29d is possible to be formed. The stick diagram of Fig. 1.29c, which was calculated by the layered antiferromagnet mentioned above, reproduced the observed data. Because the magnetic ordering of $\text{Rb}_{0.58}\text{Mn}[\text{Fe}(\text{CN})_6]_{0.86} \cdot 2.3\text{H}_2\text{O}$ is considered to be the same as that of the PI phase in $\text{Rb}_{0.88}\text{Mn}[\text{Fe}(\text{CN})_6]_{0.96} \cdot 0.5\text{H}_2\text{O}$, the PI phase should be a layered antiferromagnet.

Mechanism of Visible-Light Reversible Photomagnetism

The observed reversible photomagnetic effect can be explained by the scheme shown in Fig. 1.30. Irradiating with $h\nu$ excites the MM'CT ($\text{Fe}^{\text{II}} \rightarrow \text{Mn}^{\text{III}}$) band, which then excites the LT phase to photoexcited state I. Photoexcited

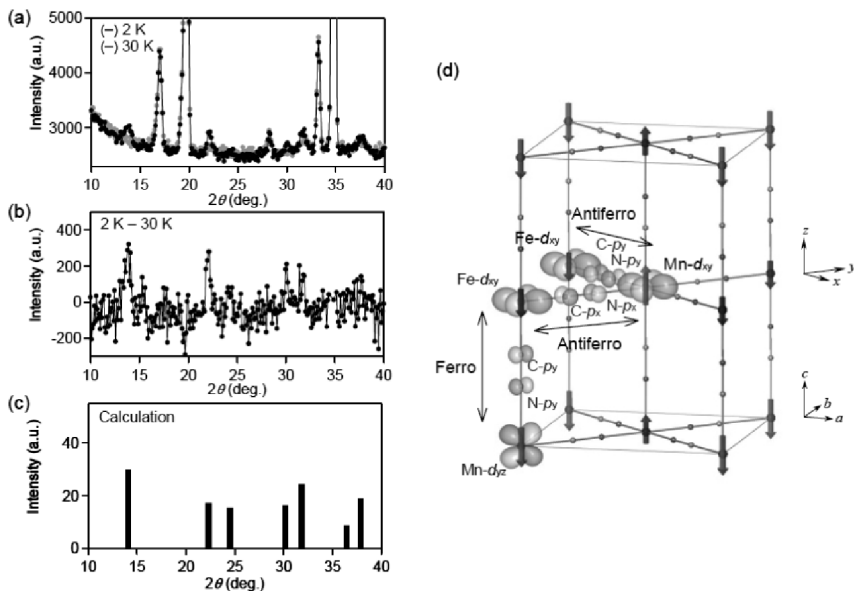


Fig. 1.29. (a) Neutron powder diffraction patterns at 2 K (*black line*) and 30 K (*gray line*). (b) Magnetic Bragg reflections as the difference in the neutron powder diffraction patterns at 2 and 30 K. (c) Calculated intensities of the magnetic Bragg reflections with an antiferromagnetic spin ordering. (d) Schematic illustration of the spin ordering. *Gray* and *Dark gray* arrows indicate the spins on Mn^{II} and Fe^{III}, respectively. From the view of the superexchange pathway, an antiferromagnetic coupling operates between Fe- d_{xy} and Mn- d_{xy} magnetic orbitals in the xy (ab) plane. In contrast, a ferromagnetic coupling operates between Fe- d_{xy} and all the d orbitals of Mn (here, Mn- d_{yz} is depicted) along the z (c) axis

state **I** proceeds to the PI phase, which has the same valence state as the HT phase. Thermal energy then suppresses the relaxation of the metastable PI phase to the stable LT phase. In contrast, the excitation of the LMCT ($\text{CN}^- \rightarrow \text{Fe}^{\text{III}}$) band of $[\text{Fe}(\text{CN})_6]^{3-}$ by irradiating with $h\nu$ excites the PI phase to photoexcited state **III**, which then proceeds to the LT phase. The LT phase is a ferromagnet due to the ferromagnetic coupling between the Mn^{III} ($S = 2$) sites, but the PI phase is an antiferromagnet. Hence, the magnetization value changes by optical switching between the LT phase and the PI phase.

A visible light-induced reversible photomagnetism between the ferromagnetic and antiferromagnetic phases is observed in a rubidium manganese hexacyanoferrate, $\text{Rb}_{0.88}\text{Mn}[\text{Fe}(\text{CN})_6]_{0.96} \cdot 0.5\text{H}_2\text{O}$, by alternately irradiating with 532 and 410 nm lights. Optical switching from the LT phase to the PI phase occurs through a $\text{Fe}^{\text{II}} \rightarrow \text{Mn}^{\text{III}}$ MMCT transition, causing photodemagnetization. In contrast, the reverse process is caused by an optical transition from the PI phase to the LT phase through a $\text{CN}^- \rightarrow \text{Fe}^{\text{III}}$ LMCT transition. The

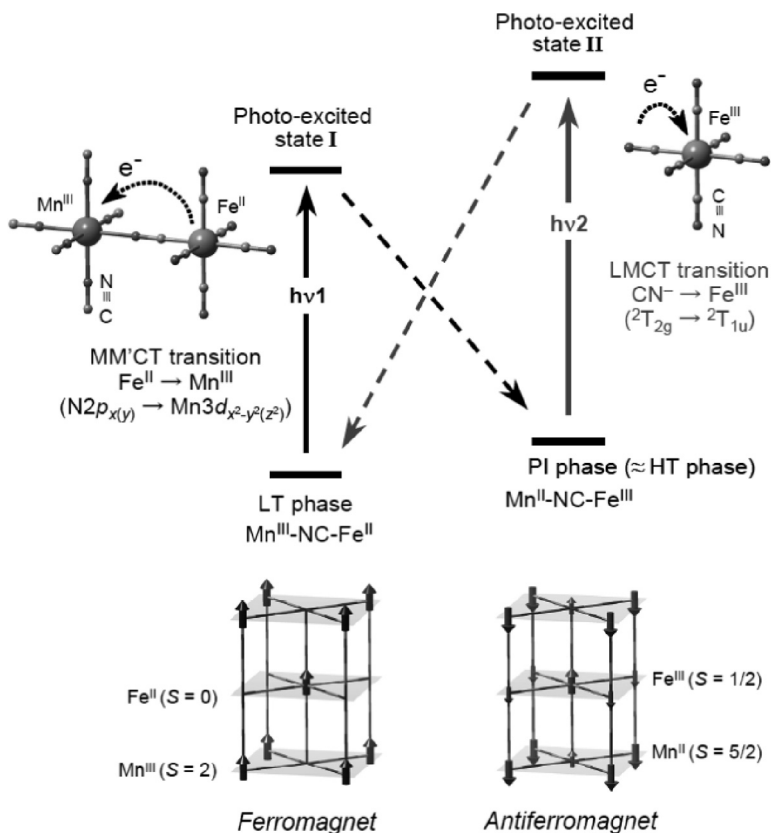


Fig. 1.30. Schematic illustration of the visible-light reversible photomagnetic effect in rubidium manganese hexacyanoferrate. Scheme for reversible charge-transfer between and (*upper*) and the spin ordering for the LT and PI phases (*lower*). LT phase is a ferromagnet due to ferromagnetic coupling between the sites, whereas the PI phase is an antiferromagnet. *Arrows* on the LT phase represent the spins of. *Large* and *small arrows* on the PI phase indicate the spins of and, respectively

existence of a photo-stationary state between the LT \rightarrow PI phase and the PI \rightarrow LT phase is also confirmed by the light source changing experiment. Although photomagnetism has been observed in some compounds, this is the first example of optical switching between a ferromagnet and an antiferromagnet.

1.10 Summary

In conclusion, a temperature-induced phase transition between the high-temperature (HT) and low-temperature (LT) phases is observed with a thermal hysteresis loop of 75 K in $\text{RbMn}[\text{Fe}(\text{CN})_6]$. The charge transfer from Mn^{II}

to Fe^{III} that accompanies the Jahn–Teller effect on the $\text{Mn}^{\text{III}}\text{N}_6$ moiety explains this phase transition. By control the x of $\text{Rb}_x\text{Mn}[\text{Fe}(\text{CN})_6]_{(x+2)/3} \cdot z\text{H}_2\text{O}$, we found that $\text{Rb}_{0.64}\text{Mn}[\text{Fe}(\text{CN})_6]_{0.88} \cdot 1.7\text{H}_2\text{O}$ exhibits a surprisingly large thermal hysteresis loop of 138 K. A hidden stable phase of HT phase, which is experimentally observed in this system, is well explained by a SD model under thermal equilibrium condition. In addition, with non phase transition material of $\text{Rb}_{0.43}\text{Mn}[\text{Fe}(\text{CN})_6]_{0.81} \cdot 3\text{H}_2\text{O}$, the *light-induced phase collapse* (LIPC) was realized. The LIPC is caused by blue-light irradiation inducing the transition from a *thermodynamically metastable phase* to a *hidden stable phase* in a material that does not undergo a thermal phase transition. Since the present phenomenon is driven only by the blue-light irradiation, it may provide a good strategy for the next generation of optical recording. As photo-induced phase transition at room temperature, the photoconversion from the LT to HT phases is observed inside the thermal hysteresis loop with a large Φ value of 38, by a one-shot-laser-pulse irradiation. This large yield and fast response will allow us to consider a new type of optical switching device. As photomagnetic effect at low temperature, the rapid- photodemagnetization has been observed by a one-shot-pulsed-laser light irradiation. With cw lights, a visible light-induced reversible photomagnetism between the ferromagnetic and antiferromagnetic phases is observed, by alternately irradiating with 532 nm and 410 nm lights. These temperature- and photo-induced phase transition phenomena are caused by: (1) the change in valence states on transition metal ions due to metal-to-metal charge-transfer and (2) the bistability due to the Jahn–Teller distortion of Mn^{III} ion.

Acknowledgements

The authors would like to thank Professor Yutaka Moritomo (University of Tsukuba) and Professor Kenji Ohoyama (Tohoku University) for the measurement of neutron powder diffraction. The present research is supported in part by a Grant-in-Aid for Young Scientists (S) from JSPS, a Grant for the GCOE Program “Chemistry Innovation through Cooperation of Science and Engineering”, the photon Frontier Network Program from the MEXT, and PRESTO JST, Japan.

References

1. O. Kahn, *Molecular Magnetism* (VCH, New York, 1993)
2. K. Nasu, *Relaxations of Excited States and Photo-Induced Structural Phase Transitions* (Springer-Verlag, Berlin, 1997)
3. P. Gutlich, A. Hauser, H. Spiering, *Angew. Chem. Int. Ed. Engl.* **33**, 2024 (1994)
4. S. Ohkoshi, K. Hashimoto, *J. Photochem. Photobio. C* **2**, 71 (2001)
5. J.F. Letard, P. Guionneau, E. Codjovi, O. Lavastre, G. Bravic, D. Chasseau, O. Kahn, *J. Am. Chem. Soc.* **119**, 10861 (1997)

6. G.A. Renovitch, W.A. Baker, *J. Am. Chem. Soc.* **89**, 6377 (1967)
7. M. Sorai, *Bull. Chem. Soc. Jpn.* **74**, 2223 (2001)
8. K. Prassides, *Mixed Valency Systems, Applications in Chemistry, Physics and Biology* (NATO ASI, Kluwer, Dordrecht, 1991)
9. M.B. Robin, P. Day, *Adv. Inorg. Chem. Radiochem.* **10**, 247 (1967)
10. N.S. Hush, *Prog. Inorg. Chem.* **8**, 391 (1967)
11. S.B. Piepho, E.R. Krausz, P.N. Schatz, *J. Am. Chem. Soc.* **10**, 2996 (1978)
12. R.D. Cannon, L. Montri, D.B. Brown, K.M. Marshall, C.M. Elliot, *J. Am. Chem. Soc.* **106**, 2591 (1984)
13. H. Kitagawa, T. Mitani, *Coord. Chem. Rev.* **190**, 1169 (1999)
14. O.S. Jung, D.H. Jo, Y.A. Lee, B.J. Conklin, C.G. Pierpont, *Inorg. Chem.* **36**, 19 (1997)
15. N. Shimamoto, S. Ohkoshi, O. Sato, K. Hashimoto, *Inorg. Chem.* **41**, 678 (2002)
16. R.J. Zimmermann, *Phys. Chem. Solids.* **44**, 151 (1983)
17. T.J. Kambara, *Phys. Soc. Jpn.* **49**, 1806 (1980)
18. S. Ohnishi, S. Sugano, *J. Phys. C* **14**, 39 (1981)
19. A. Ludi, H.U. Gudel, *Struct. Bonding (Berlin)* **14**, 1 (1973)
20. M. Verdaguer, T. Mallah, V. Gadet, I. Castro, C. Helary, S. Thiebaut, P. Veillet, *Conf. Coord. Chem.* **14**, 19 (1993)
21. S. Ohkoshi, K. Hashimoto, *Electrochem. Soc. Interface Fall* **34**, (2002)
22. T. Mallah, S. Thiebaut, M. Verdaguer, P. Veillet, *Science* **262**, 1554 (1993)
23. W.R. Entley, G.S. Girolami, *Science* **268**, 397 (1995)
24. S. Ferlay, T. Mallah, R. Ouahes, P. Veillet, M. Verdaguer, *Nature* **378**, 701 (1995)
25. S. Ohkoshi, T. Iyoda, A. Fujishima, K. Hashimoto, *Phys. Rev. B* **56**, 11642 (1997)
26. S. Ohkoshi, A. Fujishima, K. Hashimoto, *J. Am. Chem. Soc.* **120**, 5349 (1998)
27. O. Hatlevik, W.E. Bushmann, J. Zhang, J.L. Manson, J.S. Miller, *Adv. Mater.* **11**, 914 (1999)
28. S.M. Holmes, G.S. Girolami, *J. Am. Chem. Soc.* **121**, 5593 (1999)
29. S. Ohkoshi, Y. Abe, A. Fujishima, K. Hashimoto, *Phys. Rev. Lett.* **82**, 1285 (1999)
30. S. Ohkoshi, K. Arai, Y. Sato, K. Hashimoto, *Nat. Mater.* **3**, 857 (2004)
31. S. Margadonna, K. Prassides, A.N. Fitch, *J. Am. Chem. Soc.* **126**, 15390 (2004)
32. S.S. Kaye, J.R. Long, *J. Am. Chem. Soc.* **127**, 6506 (2005)
33. A.L. Goodwin, K.W. Chapman, C.J. Kepert, *J. Am. Chem. Soc.* **127**, 17980 (2005)
34. S. Ohkoshi, H. Tokoro, T. Matsuda, H. Takahashi, H. Irie, K. Hashimoto, *Angew. Chem. Int. Ed.* **3**, 857 (2007)
35. S. Ohkoshi, S. Yoroazu, O. Sato, T. Iyoda, A. Fujishima, K. Hashimoto, *Appl. Phys. Lett.* **70**, 1040 (1997)
36. A. Bleuzen, C. Lomenech, V. Escax, F. Villain, F. Varret, C.C.D. Moulin, M. Verdaguer, *J. Am. Chem. Soc.* **122**, 6648 (2000)
37. O. Sato, S. Hayami, Y. Einaga, Z.Z. Gu, *Bull. Chem. Soc. Jpn.* **76**, 443 (2003); H. Tokoro, S. Ohkoshi, K. Hashimoto, *Appl. Phys. Lett.* **82**, 1245 (2003)
38. H. Tokoro, S. Ohkoshi, K. Hashimoto, *Appl. Phys. Lett.* **82**, 1245 (2003)
39. S. Ohkoshi, N. Machida, Z.J. Zhong, K. Hashimoto, *Synth. Met.* **122**, 523 (2001)
40. G. Rombaut, M. Verelst, S. Golhen, L. Ouahab, C. Mathoniere, O. Kahn, *Inorg. Chem.* **40**, 1151 (2001)

41. J.M. Herrera, V. Marvaud, M. Verdaguer, J. Marrot, M. Kalisz, C. Mathoniere, *Angew. Chem. Int. Ed.* **43**, 5468 (2004)
42. S. Ohkoshi, H. Tokoro, T. Hozumi, Y. Zhang, K. Hashimoto, C. Mathoniere, I. Bord, G. Rombaut, M. Verelst, C.C.D. Moulin, F. Villain, *J. Am. Chem. Soc.* **128**, 270 (2006)
43. S. Ohkoshi, S. Ikeda, T. Hozumi, T. Kashiwagi, K. Hashimoto, *J. Am. Chem. Soc.* **128**, 5320 (2006)
44. S. Ohkoshi, Y. Hamada, T. Matsuda, Y. Tsunobuchi, H. Tokoro, *Chem. Mater.* **20**, 3048 (2008)
45. N. Yamada, E. Ohno, K. Nishiuchi, N. Akahira, M. Takao, *J. Appl. Phys.* **69**, 2849 (1991)
46. A.V. Kolobov, P. Fons, A.I. Frenkel, A.L. Ankudinov, J. Tominaga, T. Uruga, *Nat. Mater.* **3**, 703 (2004)
47. M. Wuttig, N. Yamada, *Nat. Mater.* **6**, 824 (2007)
48. S. Decurtins, P. Gutlich, C.P. Kohler, H. Spiering, A. Hauser, *Chem. Phys. Lett.* **105**, 1 (1984)
49. J.F. Letard, J.A. Real, N. Moliner, A.B. Gaspar, L. Capes, O. Cadpr, O. Kahn, *J. Am. Chem. Soc.* **121**, 10630 (1999)
50. S. Koshihara, Y. Tokura, T. Mikami, G. Saito, T. Koda, *Phys. Rev. B* **42**, 6853 (1990)
51. E. Collet, M.H. Lemee-Cailleau, M.B.L. Cointe, H. Cailleau, M. Wulff, T. Luty, S. Koshihara, M. Meyer, L. Toupet, P. Rabiller, S. Techert, *Science* **300**, 612 (2003)
52. M. Fiebig, K. Miyano, Y. Tomioka, Y. Tokura, *Science* **280**, 1925 (1998)
53. N. Takubo, I. Onishi, K. Takubo, T. Mizokawa, K. Miyano, *Phys. Rev. Lett.* **101**, 177403 (2008)
54. H. Tokoro, M. Shiro, K. Hashimoto, S. Ohkoshi, *Z. Anorg. Allg. Chem.* **633**, 1134 (2007)
55. S. Ohkoshi, H. Tokoro, M. Utsunomiya, M. Mizuno, M. Abe, K. Hashimoto, *J. Phys. Chem. B* **106**, 2423 (2002)
56. H. Tokoro, S. Ohkoshi, T. Matsuda, K. Hashimoto, *Inorg. Chem.* **43**, 5231 (2004)
57. H. Osawa, T. Iwazumi, H. Tokoro, S. Ohkoshi, K. Hashimoto, H. Shoji, E. Hirai, T. Nakamura, S. Nanao, Y. Isozumi, *Solid State Commun.* **125**, 237 (2003)
58. T. Yokoyama, H. Tokoro, S. Ohkoshi, K. Hashimoto, K. Okamoto, T. Ohta, *Phys. Rev. B* **66**, 184111 (2002)
59. S. Ohkoshi, T. Nuida, T. Matsuda, H. Tokoro, K. Hashimoto, *J. Mater. Chem.* **5**, 3291 (2005)
60. K. Kato, Y. Moritomo, M. Takata, M. Sakata, M. Umekawa, N. Hamada, S. Ohkoshi, H. Tokoro, K. Hashimoto, *Phys. Rev. Lett.* **91**, 255502 (2003)
61. H. Tokoro, S. Ohkoshi, T. Matsuda, T. Hozumi, K. Hashimoto, *Chem. Phys. Lett.* **388**, 379 (2004).
62. T. Nakamoto, Y. Miyazaki, M. Itoi, Y. Ono, N. Kojima, M. Sorai, *Angew. Chem. Int. Ed.* **40**, 4716 (2001)
63. H.M.J. Blote, *Physica B* **79B**, 427 (1975)
64. T. Matsumoto, Y. Miyazaki, A.S. Albrecht, C.P. Landee, M.M. Turnbull, M. Sorai, *J. Phys. Chem. B* **104**, 9993 (2000).
65. R.L. Carlin, *Magnetochemistry* (Springer, New York, 1986)
66. L.J.D. Jongh, A.R. Miedema, *Adv. Phys.* **23**, 1 (1974)

67. M.A. Subramanian, A.P. Ramirez, W.J. Marshall, *Phys. Rev. Lett.* **82**, 1558 (1999)
68. N. Ohmae, A. Kajiwara, Y. Miyazaki, M. Kamachi, M. Sorai, *Thermochim. Acta* **267**, 435 (1995)
69. B. Mayoh, P. Day, *J. Chem. Soc. Dalton.* **15**, 1483 (1976)
70. H. Tokoro, S. Miyashita, K. Kazuhito, S. Ohkoshi, *Phys. Rev. B* **73**, 172415 (2006)
71. C.P. Slichter, H.G. Drickamer, *J. Chem. Phys.* **56**, 2142 (1972)
72. K.P. Purcell, M.P. Edwards, *Inorg. Chem.* **23**, 2620 (1984)
73. H. Tokoro, S. Ohkoshi, *Appl. Phys. Lett.* **93**, 021906 (2008)
74. H. Tokoro, T. Matsuda, K. Hashimoto, S. Ohkoshi, *J. Appl. Phys.* **97**, 10M508 (2005)
75. H. Tokoro, K. Hashimoto, S. Ohkoshi, *J. Magn. Magn. Mater.* **310**, 1422 (2007)
76. S. Ohkoshi, H. Tokoro, K. Hashimoto, *Coord. Chem. Rev.* **249**, 1830 (2005)
77. H. Tokoro, T. Matsuda, T. Nuida, Y. Moritomo, K. Ohoyama, E.D.L. Dangui, K. Boukheddaden, S. Ohkoshi, *Chem. Mater.* **20**, 423 (2008)



<http://www.springer.com/978-3-642-03950-8>

Progress in Nano-Electro-Optics VII
Chemical, Biological, and Nanophotonic Technologies for
Nano-Optical Devices and Systems
(Ed.)M. Ohtsu
2010, XIV, 149 p. 100 illus., Hardcover
ISBN: 978-3-642-03950-8